AIAA SciTech Forum
12-16 January 2026, Orlando, FL
AIAA SCITECH 2026 Forum

10.2514/6.2026-0928

Temporal Anti-aliasing Method for High Speed Imaging of Hall Effect Thrusters

Miron F. Liu*
University of Michigan, Ann Arbor, Michigan, 48105

Wensheng Huang† and Matthew J. Baird‡
NASA Glenn Research Center, Cleveland, Ohio, 44135

Benjamin A. Jorns§
University of Michigan, Ann Arbor, Michigan, 48105

A temporal anti-aliasing technique for detecting plasma oscillations beyond the Nyquist limit of high-speed diagnostics is applied to imaging datasets taken of the Advanced Electric Propulsion System (AEPS) Engineering Test Unit 2 (ETU2) operating at the 600 V, 12.5 kW condition in Vacuum Facility 5 (VF-5). The theoretical underpinnings of the algorithm are presented, and the technique is first demonstrated on synthetic data. Spectral analysis of high-speed imaging data is performed at multiple sampling frequencies. In addition to global and cathode-localized modes, potentially aliased frequencies are identified and cross-checked against camera artifacts, leading to the detection of a 1.46 MHz global mode. This temporal anti-aliasing technique thus demonstrates potential to extend the frequency range of diagnostics beyond their Nyquist limit by combining datasets through a Bayesian inference framework.

I. Introduction

Passive high-speed imaging (HSI) has been employed as an optical diagnostic technique to interrogate many high-frequency phenomena in Hall thruster and hollow cathode plasmas [1–4]. Its relative ease of use, non-intrusive nature, and high spatial resolution – typically on the order of a millimeter or less per pixel – have established HSI as a popular complement to physical probes [5]. However, despite the relatively high frame rates of typical HSI systems (100 kHz range), many high-frequency oscillations in electric propulsion (EP) devices occur well beyond the Nyquist frequency of these diagnostics [6–8]. Oscilloscopes used to monitor discharge voltage and current oscillations have bandwidths extending into the tens or hundreds of megahertz and can capture high-frequency thruster oscillations, but these measurements lack spatial resolution and therefore cannot be used to characterize wave dispersion, which is necessary for identifying propagating modes. Physical wave probes may be leveraged to extract length-scale information and, in turn, allow the measurement of wave dispersion and thus the identification of the types of waves present [7, 9–11]. However, physical probes are inherently perturbative. In addition, spatial aliasing effects arising from the finite spacing between wave probe elements impose a spatial bandwidth limit on conventional two-element wave probes [9, 11, 12].

HSI addresses some shortcomings of the aforementioned diagnostic tools. In principle, individual pixels can function as non-intrusive "optical" probes, with light intensity serving as a proxy for line-integrated plasma density. Unlike physical probes, these optical probe elements can be positioned arbitrarily close to one another without introducing the risk of electrical cross-talk. Thus, given sufficiently high spatial resolution of the imaging frame, i.e. the effective inter-pixel spacing is small relative to the wavelength scales of interest, the issue of spatial aliasing is largely mitigated. However, the *temporal* frequency bandwidth constraint imposed by the slow frame rate relative to the short timescales of some plasma phenomena remains a limitation of the technique. In the absence of imaging systems capable of operating at higher frame rates, there is an apparent need to develop diagnostic methodologies that can enable the detection of high-frequency signals from data acquired at sub-Nyquist sampling rates. In light of this, we adapt a *spatial* anti-aliasing technique previously developed by Liu and Jorns and present the theoretical underpinnings of a new *temporal* anti-aliasing framework that leverages multiple HSI datasets to identify potential high-frequency modes existing at frequencies greater than the Nyquist frequency of HSI cameras [13].

*PhD Candidate, Department of Aerospace Engineering, Student Member AIAA
†Research Engineer, Electric Propulsion Systems Branch, AIAA Associate Fellow
‡Research Engineer, Electric Propulsion Systems Branch
§Associate Professor, Aerospace Engineering, AIAA Associate Fellow

With this purpose in mind, this paper is organized as follows: in section II we discuss the theoretical underpinnings of our methodology to infer high-frequency signals from multiple low-frequency datasets and present simulation results of the temporal anti-aliasing algorithm applied to synthetic data as an initial proof-of-concept of the technique. We describe the test article, diagnostic, and dataset in section III. In section IV we present results of the anti-aliasing algorithm applied to HSI datasets, followed by a discussion of the findings in section V. We conclude with a summary of the work and key insights gained in section VI.

II. Approach

Despite the high frame rates of cameras employed for HSI, on the timescales of some plasma oscillations, the maximum sampling rate offered by this approach is comparatively low relative to probe-based diagnostics. This frequency constraint stands as one of the key limitations that have prohibited HSI from resolving high frequency plasma waves. We detail in this section a framework that, in theory, mitigates this constraint and allows for the reconstruction of high-frequency signals from multiple sub-Nyquist sampling datasets. This "temporal anti-aliasing" framework can, in principle, be employed to extend the frequency range of HSI beyond their Nyquist limit.

A. Aliasing of high-frequency signal as a result of undersampling

Per the Whittaker-Nyquist-Shannon sampling theorem [14–16], sampling a periodic signal (f_g) at rate (f_s) below the Nyquist frequency ($f_{nyq} = \frac{f_g}{2}$) manifests a detected signal at a folded, alias frequency (f_a) given by [17]:

$$f_a = \left| f_g - n f_s \right|, \qquad \text{where} \qquad n = \left\lfloor \frac{f_g}{f_s} + \frac{1}{2} \right\rfloor. \tag{1}$$

In other words, when a periodic signal is undersampled at rates below the Nyquist frequency, the true frequency of the signal will appear as a different, alias frequency in Fourier space. We illustrate this concept in Fig. 1.

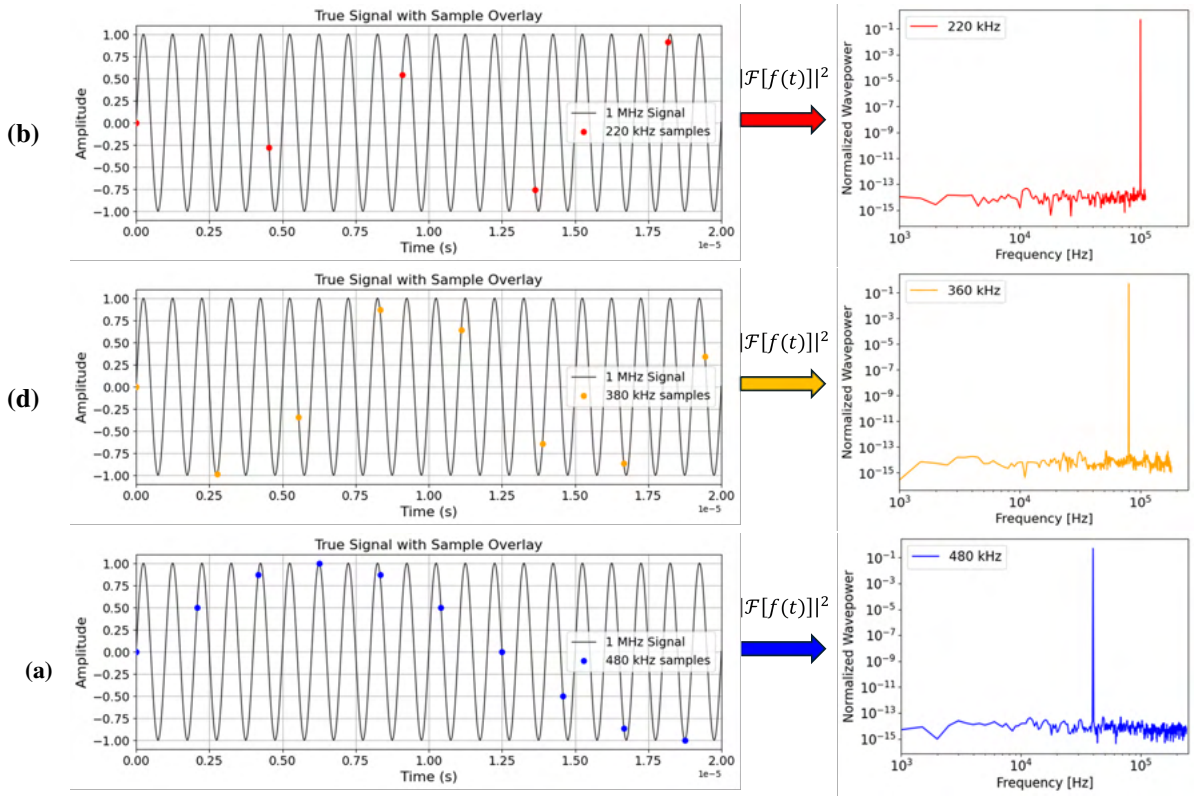

Fig. 1 1 MHz signal sampled at various frequencies with corresponding power spectra showing an aliased frequency: a) 190 kHz sampling rate, b) 280 kHz sampling rate, c) 480 kHz sampling rate

It is evident here that the true signal at 1 MHz is aliased to various frequencies on the power spectra depending on the sampling frequency, a consequence of using sampling rates below the Nyquist criterion. This phenomenon is the most

apparent in Fig. 1a where undersampling results in a visibly lower-frequency waveform. The observation that different sampling frequencies yield different frequency aliases serves as the basis for the temporal anti-aliasing framework we describe in the following.

B. Temporal anti-aliasing framework for reconstructing de-aliased dispersion plots

The analysis framework presented in this work is predicated on the principle that varying the frame rate in the presence of a high-frequency signal beyond the Nyquist limit of the camera will lead to a corresponding change in the alias frequency captured by the camera. The alias frequencies can be related to the true, aliased frequency through Eqn. 1. For clarity, in this work we use "alias" frequencies to refer to frequencies observed in data that could be attributed to aliasing, and "alias-*ed*" frequencies to refer to the true signal frequencies that have undergone frequency folding. This invites the possibility that HSI measurements obtained across multiple sampling rates can be jointly analyzed through Bayesian inference to exploit this correlation and regress a probability distribution function of the true signal frequency.

We give an overview of our temporal anti-aliasing approach here, the formalism of which closely follows the Bayesian framework developed in our previous work on spatial anti-aliasing. Indeed, the present approach is a direct adaptation from the spatial frequency focus of the previous work to temporal frequency. Readers are referred to [13] for additional details on the Bayesian methodology behind these anti-aliasing techniques. We show in Fig. 2 a notional overview of our temporal anti-aliasing approach.

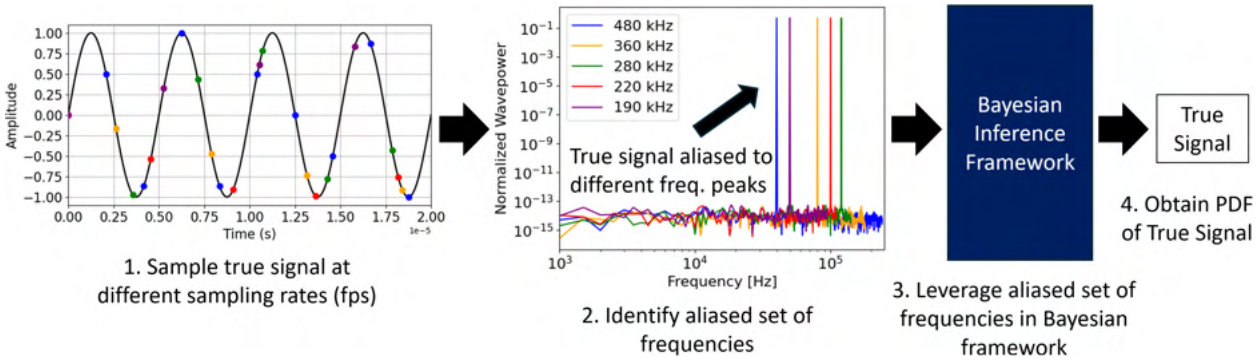

Fig. 2 Temporal anti-aliasing framework

We begin by sampling the true signal at various sampling frequencies (step 1) a statistically significant i number of times (number of time-varying traces) from which we obtain i sets of alias frequencies (step 2). At this step, any single dataset alone is insufficient to determine the real signal. This is evident by inspection of Eqn. 1 which shows that there are an infinite number of potential frequencies, spaced by integer multiples of the sampling frequency, that could be folded to the observed, alias frequency. However, we posit this can be mitigated by combining information from all of the datasets through the formulation of a likelihood function given by

$$\mathcal{L}(\bar{f}^i, \sigma_{\bar{f}^i} \mid f_g, f_s^i) = \prod_{i=1}^{N} \frac{1}{\sqrt{2\pi\sigma_{\bar{f}^i}^2}} \exp\left(-\frac{\left(h(f_g, f_s^i) - \bar{f}^i\right)^2}{2\sigma_{\bar{f}^i}^2}\right), \tag{2}$$

where $h(f_g, f_s^i)$ is a model based on the formula for folded frequency, Eq. 1, and

$$h(f_g, f_s^i) = f_a^i = |f_g - n f_s| + \xi, \qquad n = \left\lfloor \frac{f_g}{f_s} + \frac{1}{2} \right\rfloor, \qquad \xi \sim \mathcal{N}\left(0, \sigma_{\bar{f}^i}^2\right). \tag{3}$$

Here f_g is a swept free parameter denoting the true signal frequency, f_s^i are fixed model parameters representing the known sampling frequencies indexed by the trace number "i", $\bar{f}^i$ represents the observed, mean alias frequency from data and $\sigma_{\bar{f}^i}$ represents the corresponding measurement standard deviation with which we endow the model with Gaussian noise ξ distributed with zero mean and variance $\sigma_{\bar{f}^i}^2$. We have defined the overall likelihood distribution over frequency as the joint probability of Gaussian likelihoods associated with each sampling frequency dataset.

Through this prescription, even if the alias frequency observed with a single sampling frequency corresponds to an infinite set of potential aliased signal frequencies, only the *true* signal frequency will lie at the intersection between *all*

sets of possible alias frequencies observed from the various sampling rates. With every additional sampling rate, the number of possible intersections between the sets of potential frequencies will be reduced. Thus, across a finite sweep of f_g, with a sufficient number of sampling rates the number of frequency intersections should converge to 1, which will then uniquely identify the true frequency. This principle is captured by the topology of the likelihood model in which the true frequency will maximize the product of individual Gaussian likelihoods across all sampling rates.

C. Proof-of-concept demonstration on synthetic data

Prior to applying this technique to experimental data, we evaluate its efficacy by first simulating the sampling of a 1 MHz time-varying oscillation at various rates as illustrated in Fig. 1. For each dataset, we prescribe a variance equal to twice the frequency bin-width of the power spectra ($\sigma^2 \approx 1$ kHz). We see in Fig. 3 the convergence of the temporal anti-aliasing likelihood plot with more data.

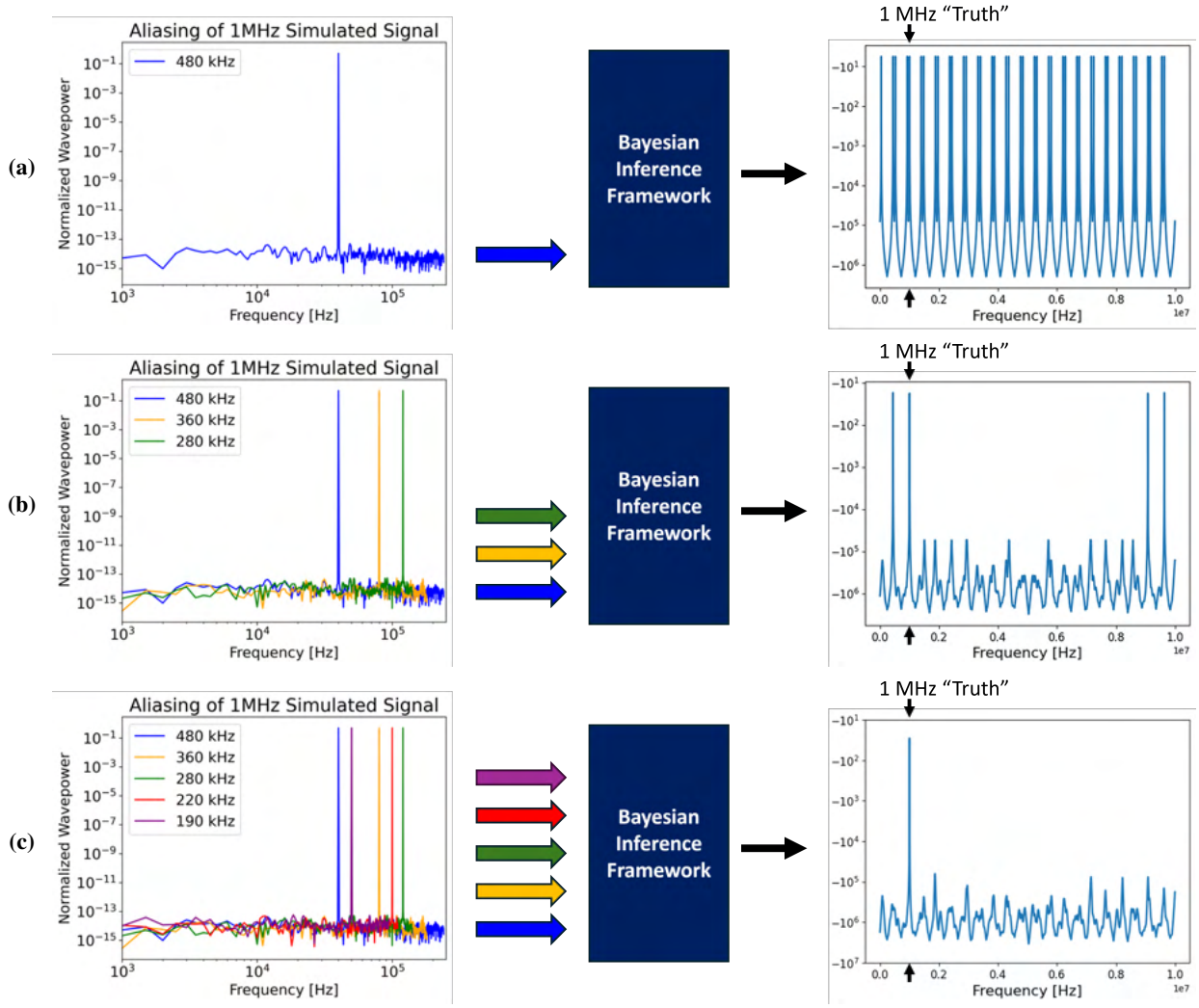

Fig. 3 Convergence of temporal anti-aliasing likelihood function to identification of the 1 MHz simulated "true signal" ($\sigma^2 \approx 1$ kHz) with increasing data: a) 1 dataset showing aliasing, b) 3 datasets showing convergence to true signal, c) 5 datasets resulting in correct identification of true signal frequency

Fig. 3a illustrates precisely the issue of aliasing with only one dataset: the likelihood plot contains an infinite series of peaks, each corresponding to a potential aliased frequency given the observed alias frequency and sampling rate. In Fig. 3b, adding additional datasets reduces the number of peaks in the likelihood function. This is an intuitive result: only frequencies existing at the intersection of all three sets of potential aliased frequencies will maximize the likelihood. Finally, with sufficient data, we see in Fig. 3c that there remains only 1 aliased frequency that can be explained by *all* of the observed alias frequencies.

III. Experimental Arrangement

In the following, we provide an overview of the test article and facility, present the experimental configuration for HSI, and identify the imaging regions of interest on which we perform spectral analysis.

A. 12.5 kW Hall Thruster Test Article and Facility

The test article shown in Figure 4 is a 12.5 kW Advanced Electric Propulsion System (AEPS) Engineering Test Unit 2 (ETU2) developed by NASA and Aerojet Rocketdyne [18]. The imaging dataset presented in this work was taken at the 600V, 12.5 kW thruster operation condition on 22 mg/s of xenon [19]. The test article was imaged in Vacuum Facility 5 (VF-5) at the NASA Glenn Research Center. This 18.3 m long by 4.6 m diameter vacuum facility provides a xenon pumping speed of 700 kL/s and achieves a typical no-load base pressure of 10^{-7} Torr-Xe.

B. High Speed Imaging System

A Photron FastCAM SA-Z Model 480k was used to image the test article head-on (Fig. 5) [19]. To increase the camera framerate, the imaging domain was reduced to only the upper half of the test article. We investigate the wave properties using pairs of "optical probes" (individual pixels) at 12 radial locations throughout the imaging domain, which we notionally show in Fig. 17. We group these point pairs into three groups: the "channel region", spanning channel centerline to the inner front pole, the "pole region" spanning points along the pole piece until the outer edge of the cathode, and the "cathode region" spanning points from the cathode outer edge to thruster centerline. For brevity, however, we only focus on the three most relevant locations in the results section of this work, shown in Fig. 6: C1 points, which are coincident with channel centerline, P2 "mid-pole points," which lie at the midpoint between channel centerline and the outer edge of the cathode, and is the location of interest for demonstrating our temporal anti-aliasing technique, and Ca1 points located near the inner edge of the inner front pole. We denote the points located along the dotted radial centerline in Fig. 6 as "center probe" points, and their nearest neighbor pixel to the left as "outer probe" points. The data for all points and imaging datasets are included in the appendix.

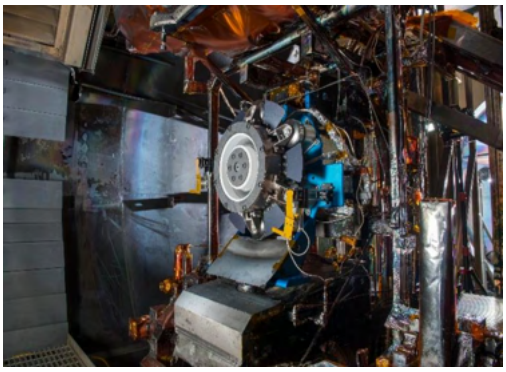

Fig. 4 ETU2 test article in VF-5 [19]

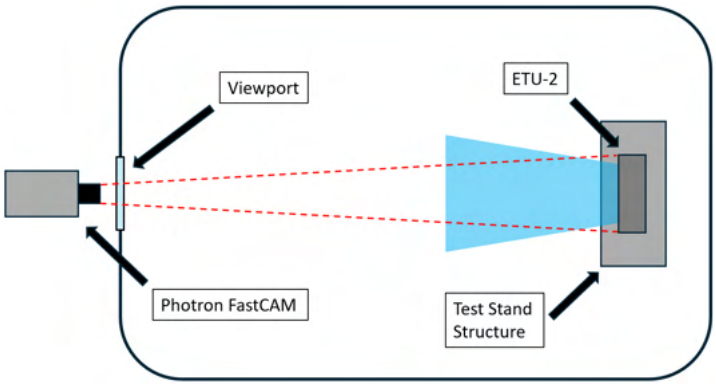

Fig. 5 VF-5 high speed imaging schematic

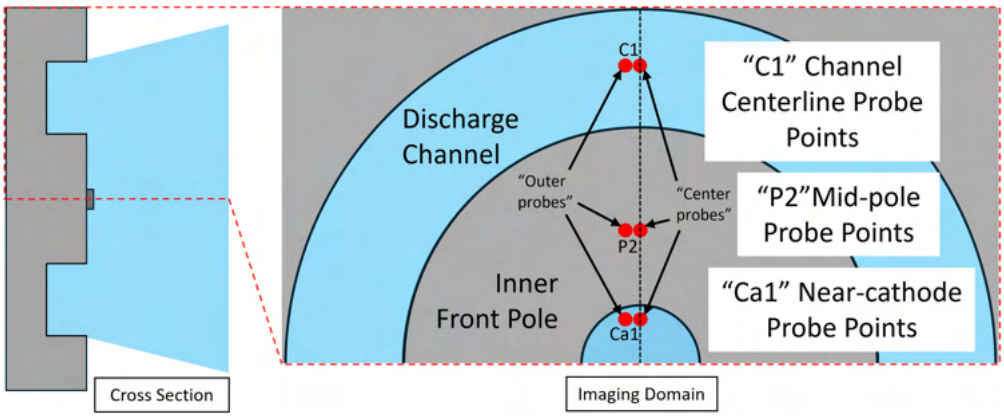

Fig. 6 Radial locations probed on imaging domain

IV. Results

In this section, we first present the spectral analysis results for the 480 kHz dataset at the C1, P2, and Ca1 locations, highlighting features associated with global and cathode modes. We then examine potentially aliased modes, followed by a discussion of camera artifacts that may contribute to the observed aliasing. Finally, we summarize the modes of interest and apply temporal anti-aliasing to identify a potentially aliased global mode.

A. Spatially-resolved power spectra and Beall plots of 480 kHz dataset

We show in Fig. 7 spectral analysis results at the C1, P2, and Ca1 pixel locations. The panels on the left show the power spectra of the oscillations, computed from the average of 91 traces, which were generated by dividing the recording into 91 different segments, while the panels on the right show the corresponding Beall plots, obtained by dividing the recording into 910 segments. This was done to create a statistically significant number of samples on which to perform Beall analysis, a histogram-based bispectral analysis technique that maps length scale information of a propagating mode to its temporal frequency. Readers are referred to our previous works [9, 11, 13, 20] and seminal work [21] for the details of this technique. In this work, each Beall plot is constructed through two-point correlation between points spaced in the azimuthal direction. These plots thus show the azimuthal wavenumber of propagating waves.

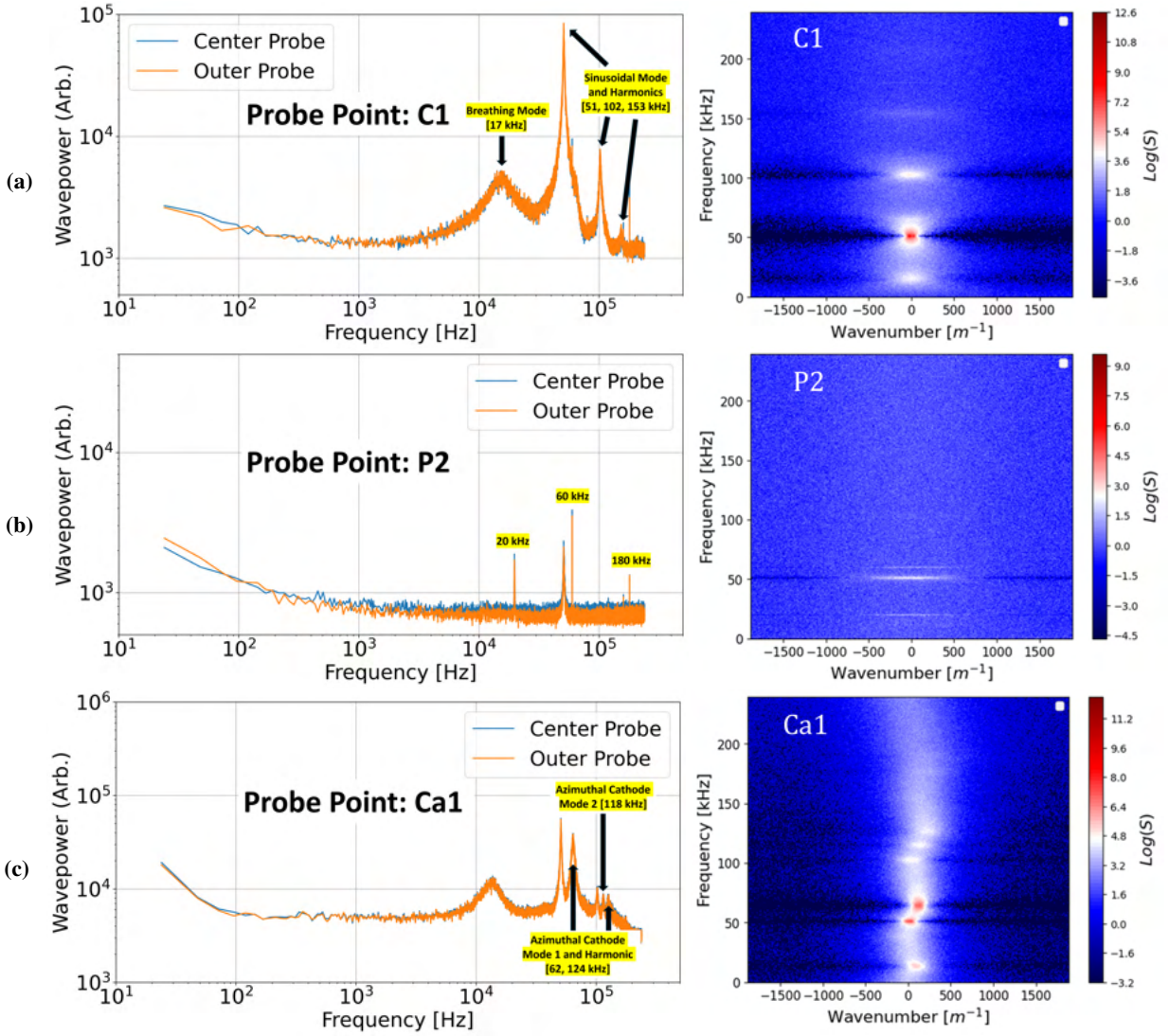

Fig. 7 480 kHz dataset spatially-resolved power spectra and Beall plots: a) Channel centerline point C1, b) Mid-pole point B2, c) Cathode-adjacent point Ca1

At the C1 location corresponding to the channel centerline, Fig. 7a, we observe a broadband feature centered at 17 kHz commensurate with the breathing mode. We also identify the sinusoidal mode, first reported in [2], along with

its harmonics at 51, 102, and 153 kHz, respectively. The associated Beall plot indicates that these modes have zero wavenumber, confirming that they are global, axial oscillations. Next, at the mid-pole point P2, Fig. 7b, the global oscillations diminish in amplitude, and three very narrow-band peaks emerge at 20, 60, and 180 kHz. The Beall plots indicate these modes are global modes. These features will be the focus of the following subsection. Finally, at the Ca1 cathode-adjacent points 7c, we observe, alongside the breathing and sinusoidal modes, the presence of an azimuthally propagating mode, indicated by its finite wavenumber on the Beall plot, at 62 kHz and its harmonic at 124 kHz. These frequencies are consistent with the rotating cathode mode reported in [22], where such a mode was first identified in a magnetically shielded hall thruster. The effective wavelength of this mode is approximately 4 mm. Interestingly, we also observe a second rotating cathode mode at 118 kHz that, to the authors' knowledge, has not previously been observed to simultaneously propagate with the lower-frequency cathode mode. The effective wavelength of this mode is approximately 10 mm. With the exception of the narrow-band features at P2, the signatures of the global and cathode modes are consistent across all probe points and frame rates indicating they are not aliased modes (see appendix).

B. Potentially aliased frequencies

We show in Fig. 8 Beall plots at the P2 location across all five HSI datasets taken at varying frame rates.

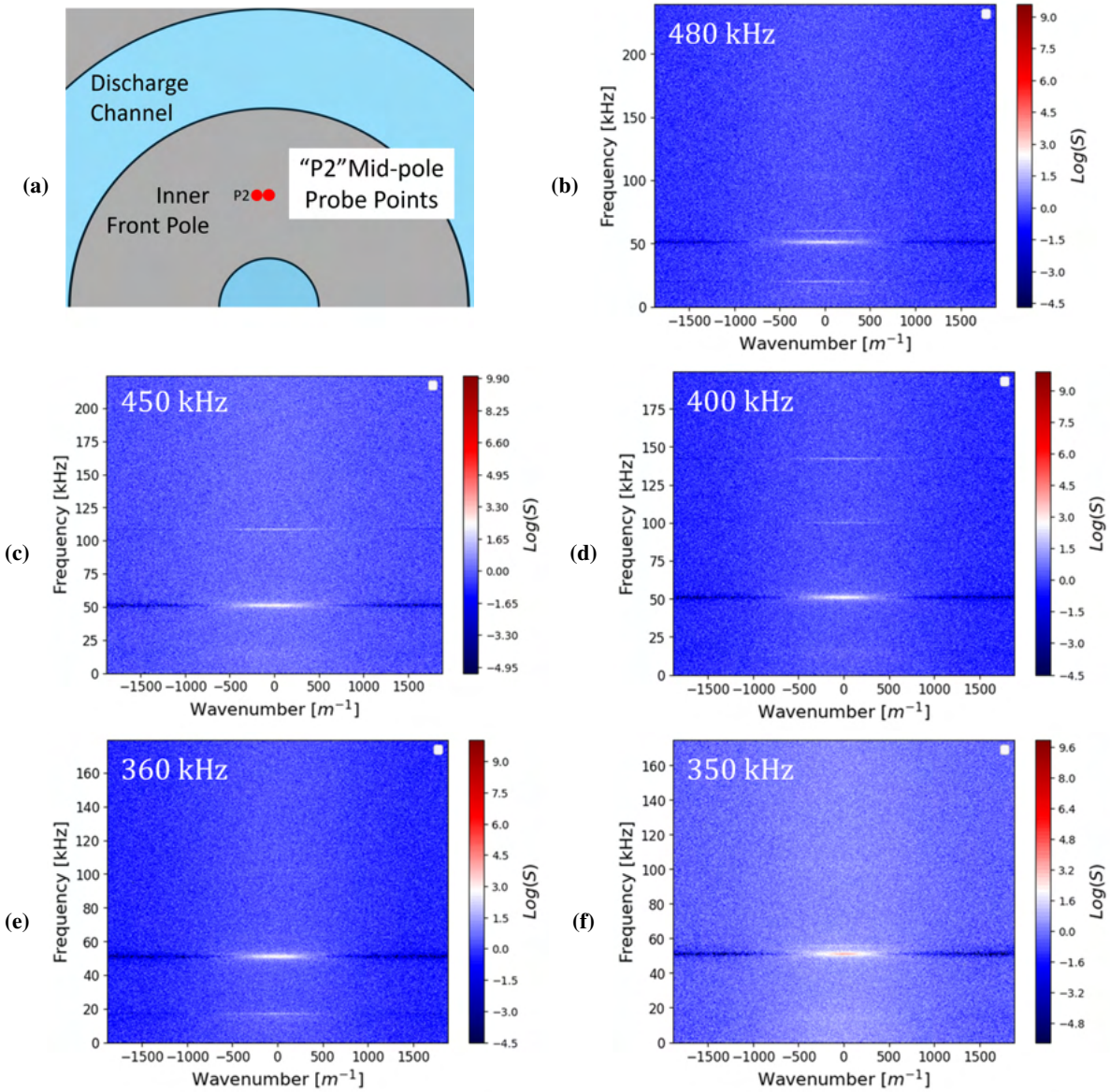

Fig. 8 Beall plots at mid-pole probe point across all fps datasets: a) Probed position b) 480 kHz dataset, c) 450 kHz dataset, d) 400 kHz dataset, e) 360 kHz dataset, f) 360 kHz dataset

We choose to inspect the mid-pole point for aliased modes since the amplitudes of global and cathode modes are reduced, which would otherwise obscure the weaker features. It is evident from these results that the narrow-band features vary in frequency depending on the imaging frame rate, a behavior consistent with temporal aliasing as described in Sec. II. At a 480 kHz sampling rate, the Beall plot shows two distinct alias frequencies at 20 and 60 kHz. At 450 kHz, only a single alias frequency appears at 110 kHz. At 400 kHz, two alias frequencies reemerge at 100 and 142 kHz. At 360 kHz, one alias frequency is observed at 17 kHz, and at 350 kHz, one appears at 57 kHz. The number of potentially alias frequencies varies across sampling rates: some datasets exhibit two frequencies, while others exhibit only one. We posit there are two possible explanations for why this may be the case. The first is that there may be more than one mode subject to temporal aliasing that happen to share a subset of aliases. Alternatively, some of these features could result from camera artifacts, a possibility we explore in the following subsection.

C. Frequencies potentially associated with camera background artifacts

To confirm whether some of the narrow-band features observed in the preceding are merely camera artifacts, we take "background shots" with the lens cover installed on the FastCAM. Capturing the background without the plasma can help us disambiguate artifacts inherent to the camera apart from real plasma phenomena. We show in Fig. 9 the results of this analysis. We average 114 traces using the trace-generation method described in IV.A, at each FPS to generate the power spectra.

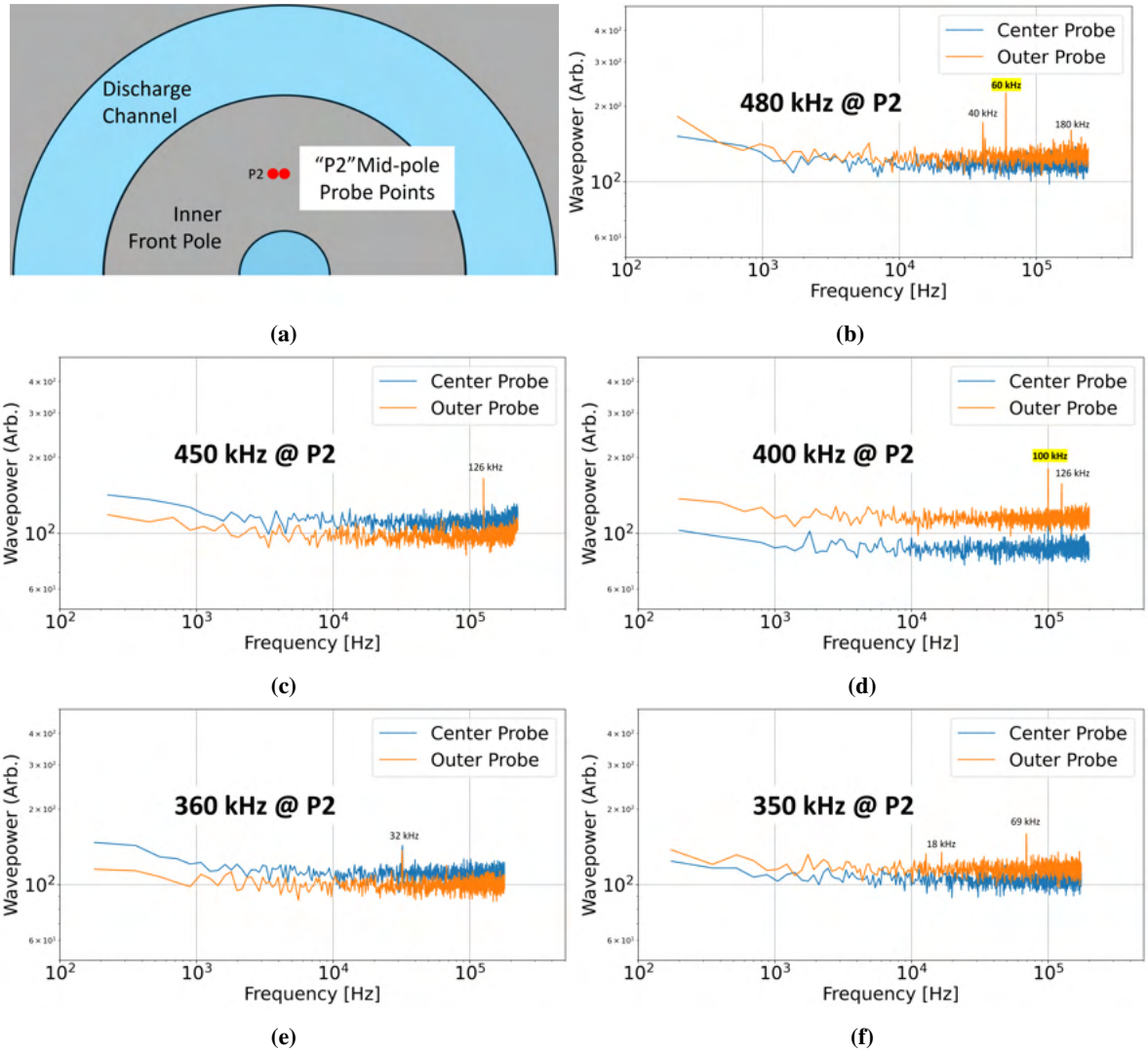

Fig. 9 Power spectra at mid-pole probe point across all fps datasets with camera lens cover on showing artifact frequencies: a) Probed position, b) 480 kHz dataset, c) 450 kHz dataset, d) 400 kHz dataset, e) 360 kHz dataset, f) 360 kHz dataset

At a 480 kHz sampling rate, the power spectra indicate three potential artifact frequencies at 40, 60, and 180 kHz. At 450 kHz, only one artifact frequency appears at 126 kHz. At 400 kHz, two artifact frequencies emerge at 100 and 126 kHz. At 360 kHz, one artifact frequency is observed at 32 kHz, and at 350 kHz, two appear at 18 and 69 kHz. We have highlighted two notable frequency artifacts. Recall from our results in the previous section that two datasets — those acquired at 480 kHz and 400 kHz — showed two potentially aliased modes. Notably, we see here that the 480 kHz background shot shows a 60 kHz artifact, and the 400 kHz background shot shows a 100 kHz artifact, which are both coincidentally one of the potentially aliased frequencies identified for these datasets in the preceding section. The remaining camera artifacts are not represented in these datasets.

D. Summary of notable frequencies and demonstration of temporal anti-aliasing

We summarize here the notable frequencies identified in our spectral analysis. Tab. 1 shows the frequencies and wavelengths associated with the global and cathode modes. For this operating condition, the breathing mode is centered around a frequency of 17 kHz with the larger amplitude sinusoidal mode and its first two harmonics existing at 51, 102, and 153 kHz. A rotating cathode wave and its first harmonic propagates at 62 and 124 kHz, alongside a second, rotating cathode mode at 118 kHz with much lower amplitude than its lower frequency counterpart.

Type	Frequency	Wavelength
Breathing Mode	17 kHz	Global
Sinusoidal Mode	51 kHz + harmonics	Global
Cathode Mode 1	62 kHz + harmonic	4 mm
Cathode Mode 2	118 kHz	10 mm

Table 1 Non-aliased Modes

Tab. 2 lists the narrow-band features observed at the P2 location, alongside the corresponding artifact frequencies identified from the camera background shots. Cross-checking the potentially aliased modes against frequencies likely associated with camera artifacts reveals a single aliased frequency per dataset: 20 kHz for the 480 kfps dataset, 110 kHz for 450 kfps, 142 kHz for 400 kfps, 17 kHz for 360 kfps, and 57 kHz for 350 kfps.

FPS	Aliased Modes	Camera Artifact Modes
480 kHz	20, ~~60~~ kHz	40, 60, 180 kHz
450 kHz	110 kHz	126 kHz
400 kHz	~~100~~, 142 kHz	100, 126 kHz
360 kHz	17 kHz	32 kHz
350 kHz	57 kHz	18 kHz, 69 kHz

Table 2 Potentially aliased modes and camera artifacts

Inputting this set of frequencies into our Bayesian anti-aliasing framework and sweeping the frequency domain up to 10 MHz in 100 Hz increments yields a peak in the likelihood function at 1.46 MHz. The log-likelihood value at this location is at least two orders of magnitude higher than any other frequency. We show this result in Fig. 10.

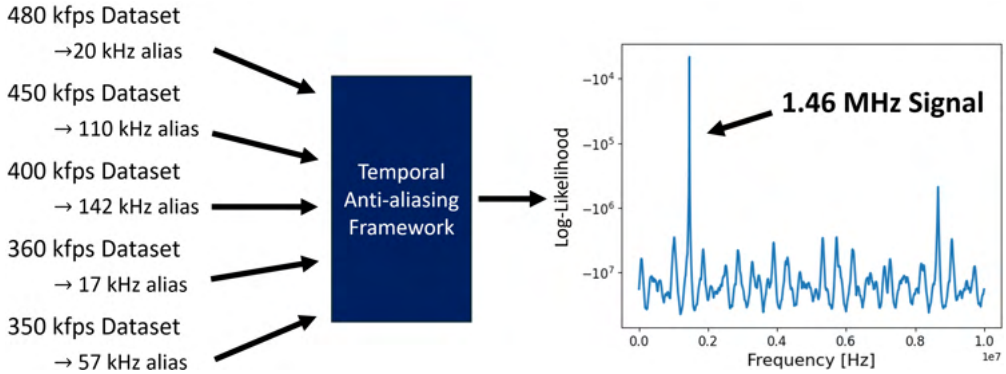

Fig. 10 Temporal anti-aliasing of HSI dataset

V. Discussion

We discuss here possible explanations for the detection of a high-frequency global mode and some confounding factors. We then describe a potential algorithm to automate the temporal anti-aliasing process, followed by preliminary validation of this algorithm on synthetic data. Lastly, we discuss the implications of this work for high speed imaging diagnostics as well as future work.

A. Detection of the 1.46 MHz mode and confounding factors

To the authors' knowledge, no narrow-band global modes in the 1–2 MHz range have been experimentally reported in Hall thrusters. While several plasma waves with MHz-range frequencies have been observed in Hall thruster and cathode plumes — such as oscillations associated with the electron cyclotron drift instability (ECDI) [23] and ion-acoustic turbulence (IAT) [9] — these phenomena follow well-defined dispersion relations and do not manifest as highly peaked, narrow band of frequencies such as the one detected in this work.

Similarly, plasma waves predicted to operate near the pole or near-plume region in the lower-MHz regime, such as the lower hybrid drift instability (LHDI) and the modified two-stream instability (MTSI), are known to propagate primarily in the azimuthal direction, rather than axially [8]. Regarding axially propagating modes, the only other well-established longitudinal oscillations aside from the breathing and sinusoidal modes are those associated with the ion transit time instability (ITTI) [24–26]. Even so, the dominant frequencies for ITTI are typically on the order of only a few hundred kilohertz. If the detected global mode is a transit time oscillation, its higher frequency suggest that either the length-scale related to the species' transit time may be shorter, and/or the velocity of the species of interest may be faster than those associated with ITTI oscillations.

We acknowledge the possibility that the 1.46 MHz feature observed here may not correspond to a real plasma behavior and could instead manifest from confounding factors. Indeed, examination of the power spectra (Fig. 11) generated from discharge current and voltage traces taken during the test reveals no narrow-band feature near 1.46 MHz, while the breathing and sinusoidal modes remain clearly resolvable. This absence is noteworthy: if a global mode at 1.46 MHz were truly present and detectable via HSI, we may expect it to appear in the discharge power spectra. Since no such feature is observed, we consider several possible explanations for the temporal anti-aliasing results.

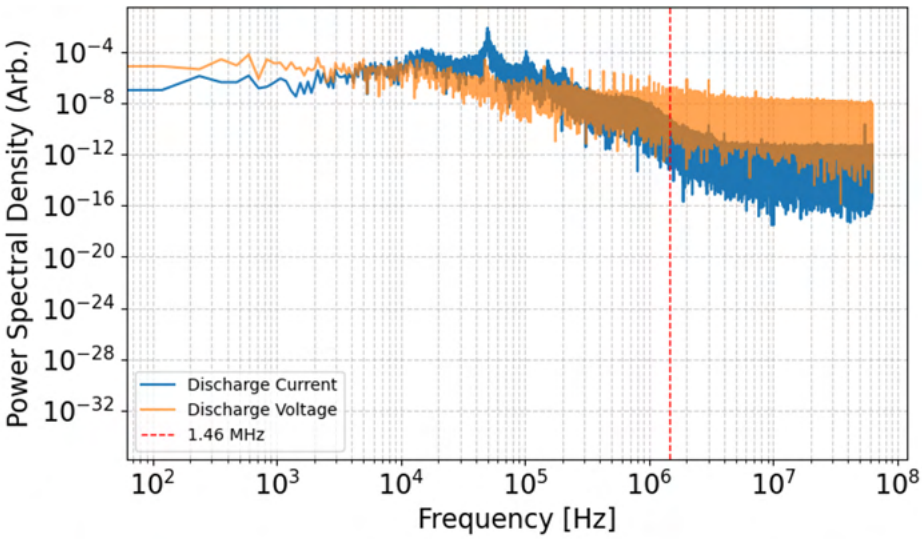

Fig. 11 Discharge current and voltage power spectra

First, ETU-2 imaging and background shots were acquired on different days. It is thus plausible that thermal drift in the camera or electronics shifted the frequencies of camera-related artifacts. This could explain why some artifact frequencies identified in background imaging did not appear in the ETU-2 datasets, and vice versa. Consequently, it remains possible that the aliased peaks observed in our measurements are entirely attributable to camera artifacts, implying that no real mode exists at 1.46 MHz.

Second, electromagnetic interference (EMI) within the laboratory environment could plausibly produce spurious peaks in the measured power spectra. This can come from various sources, such as AM radio waves that exist in the low MHz range, or RF noise associated with various power supplies in the lab environment.

Finally, mechanical vibrations in the laboratory could modulate the image at a particular frequency, leading to

a false, temporally aliased signal. Moreover, since the background shots and the ETU-2 imaging were acquired at different locations, this spatial difference could contribute to the discrepancies between the frequencies observed in the background datasets and those detected in the HSI measurements.

B. Implications for HSI analysis and future work

The application of temporal anti-aliasing in our work demonstrates that HSI can, in principle, resolve plasma oscillations beyond the Nyquist limit of high-speed cameras. By combining multiple sub-Nyquist datasets within a Bayesian framework, the frequency range can be effectively extended to infer high-frequency modes that would otherwise be inaccessible, providing a non-intrusive alternative to probe-based diagnostics for capturing both spatial and temporal information with high bandwidth.

However, the tentative detection of the 1.46 MHz feature brings to light the need for careful consideration of a few potential confounding factors that may manifest false positives for temporal anti-aliasing. We propose here potential methods to disambiguate the 1.46 MHz results from experimental artifacts. To address thermally drifting camera artifacts, background shots can be taken immediately after each imaging dataset, reducing the time for thermal drift to affect measurements. Secondly, EMI can be characterized in the laboratory space during the experiment and, if necessary, reduced through shielding of the camera and/or background-subtracted in post-processing. To address the potential for mechanical vibration to manifest as artifacts in the HSI dataset, the camera can be relocated to a low vibration environment prior to taking background shots, or mounted on vibration damping pads.

Lastly. it is important to note that, while the results of this work are promising, the current implementation of the technique relies on manual selection of alias frequencies for input into the Bayesian framework. While temporal de-aliasing spectra in the presence of one aliased mode is trivial - there will only be one alias frequency per dataset, allowing for straightforward manual selection - the task becomes rapidly intractable when multiple aliased frequencies are present (this will manifest as multiple alias peaks in each spectra). As the number of aliased modes increases, the possible permutations of alias frequency combinations increase rapidly, making selection by eye impractical. The need is apparent for an algorithm that can perform automatic temporal anti-aliasing. We detail some preliminary work on such an algorithm in the following subsections.

C. Potential method for automatic temporal anti-aliasing

To enable automatic temporal anti-aliasing, we must establish an efficient way to evaluate the likelihood that a given frequency index contains aliased power. The algorithm we propose relies on the principle that power from a high-frequency mode will be folded onto whichever lower frequency it aliases to. Mathematically,

$$P_{f,tot} = P_f + P_{fa} \tag{4}$$

where P_f is the power spectral density (PSD) at the true frequency f, and P_{fa} is the contribution to the PSD by the higher frequency that aliases to f. The observed PSD at index f is therefore the sum of the true power at that frequency and any aliased contributions. Consequently, frequency indices that exhibit anomalously elevated PSD relative to corresponding indices in other sampling-frequency datasets provide us with a signature of aliased modes. With this in mind, we will first construct a "ranking matrix" which allows us to compare the PSD value at each frequency index across all of the sampling rate datasets. We provide the algorithm used to construct such a matrix below, as well as in the corresponding illustration Fig. 12.

Part I: Ranking matrix generation

1) Image the test article at S different frequencies
2) Generate a power spectrum for each of the S datasets
3) Interpolate the frequency domain of all power spectra onto the frequency domain of the dataset taken at the lowest sampling frequency.
4) The lowest sampling frequency dataset will have F frequencies in the domain. Truncate all other spectra to this frequency domain.
5) Create a $S \times F$ "ranking matrix" where each row corresponds to a different sampling frequency, and each column corresponds to a frequency index. For each column, the elements of each matrix represents the ranking of wave power at that frequency among the various sampling rate datasets.

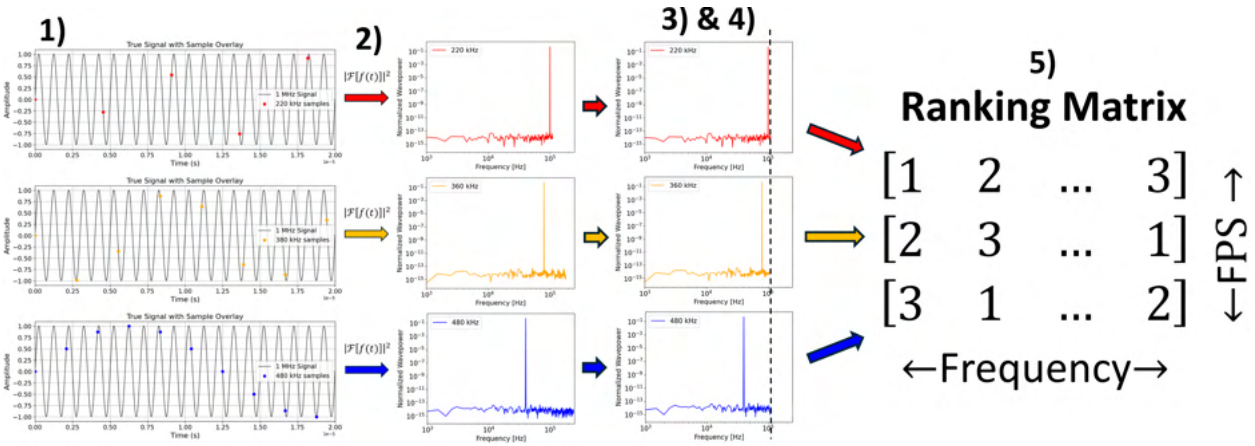

Fig. 12 Ranking matrix construction procedure

After constructing the ranking matrix, the next step is to determine the likelihood of aliased frequencies contributing to the PSD value at each frequency index. The algorithm we propose is as follows (Fig. 13):

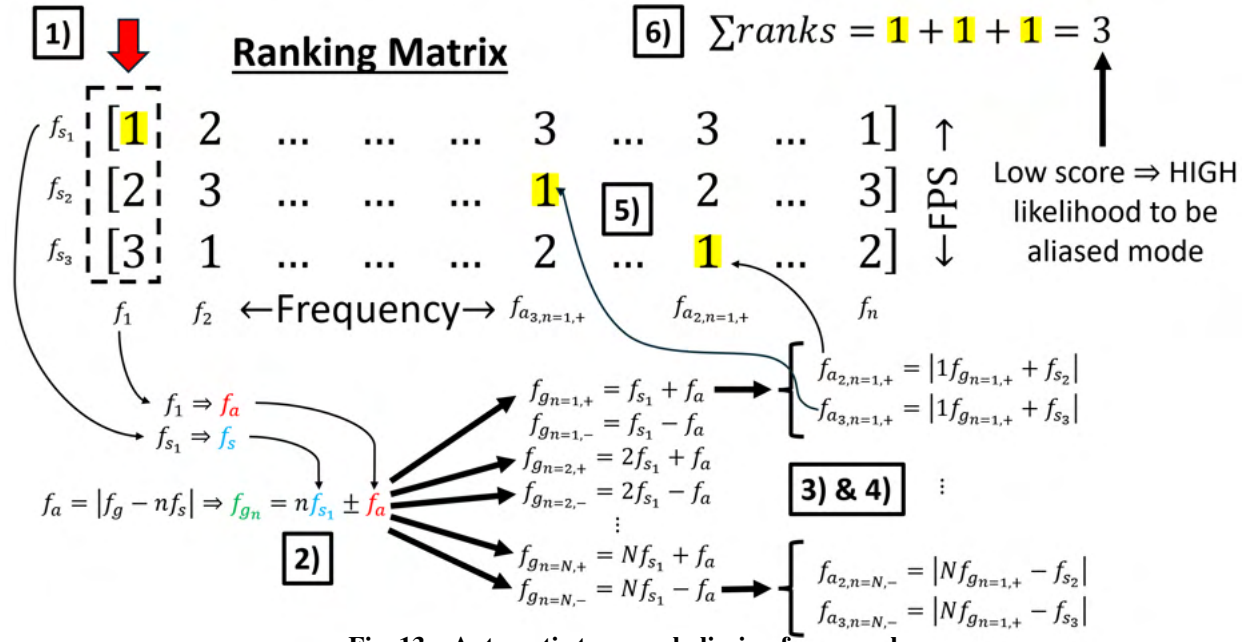

Fig. 13 Automatic temporal aliasing framework

Part II: Loop over frequency (over each column of ranking matrix)

1) Identify the row ranked highest and its corresponding sampling frequency
2) For this highest-ranked frequency f_a' and sampling frequency f_s, compute the next N nearest-neighbor aliased frequencies according to the folded frequency formula Eq. 1.
3) For each frequency f_{n_i} of the N nearest-neighbor potentially aliased frequencies
    1) Compute the frequencies f_{n_j} will alias to when sampled at each of S sampling frequencies according to the folded frequency formula Eq. 3. Here, we substitute f_{n_j} for f_g and f_{s_i} for f_s.
4) We will arrive at a $i \times j$ matrix of $f_{a_{ij}}$ alias frequencies where each of i row corresponds to sampling rate f_{s_i} and each of j column corresponds to f_{n_j} nearest-neighbor aliased frequencies
5) For each column in $f_{a_{ij}}$
    1) Find the frequency indices in the ranking matrix corresponding to each aliased frequency of column i
    2) Compute the sum/product of ranks at each index
6) Assign a likelihood weight equal to the inverse sum/product of ranks to the potentially aliased mode (lower sum/product = higher likelihood)

D. Preliminary validation of automatic temporal anti-aliasing in simulation

As a first-pass validation of our automatic temporal anti-aliasing algorithm, we simulate data acquisition of three non-aliased modes and three aliased modes at six different frequencies tabulated in Tab. 14

Sampling Frequencies		Simulated Non-aliased Modes	Simulated Aliased Modes
430 kHz	440 kHz	5 kHz	1 MHz
450 kHz	460 kHz	20 kHz	1.352 MHz
470 kHz	480 kHz	110 kHz	1.46 MHz

Table 3 Simulated Modes

We model the simulated signal of propagating waves using:

$$I(0,t) = \sum_{f=1}^{F} A sin(-\omega_f \cdot t) + \xi(t), \quad \xi \sim \mathcal{N}(0,\Gamma) \tag{5}$$

Here, A denotes the amplitude of the simulated waves, which we set to unity. The subscript f indexes the f^{th} frequency (corresponding to linear frequency f) from Tab. 14. We then perturb the signal at every timestep by adding Gaussian noise with variance Γ. The contribution to the time-varying signal from one dispersion function is obtained by summing over all frequency components $\sum_{f=1}^{F}$ of the six simulated waves. The simulation time is 2 ms, and the noise variance is set to 0.1 for the following results.

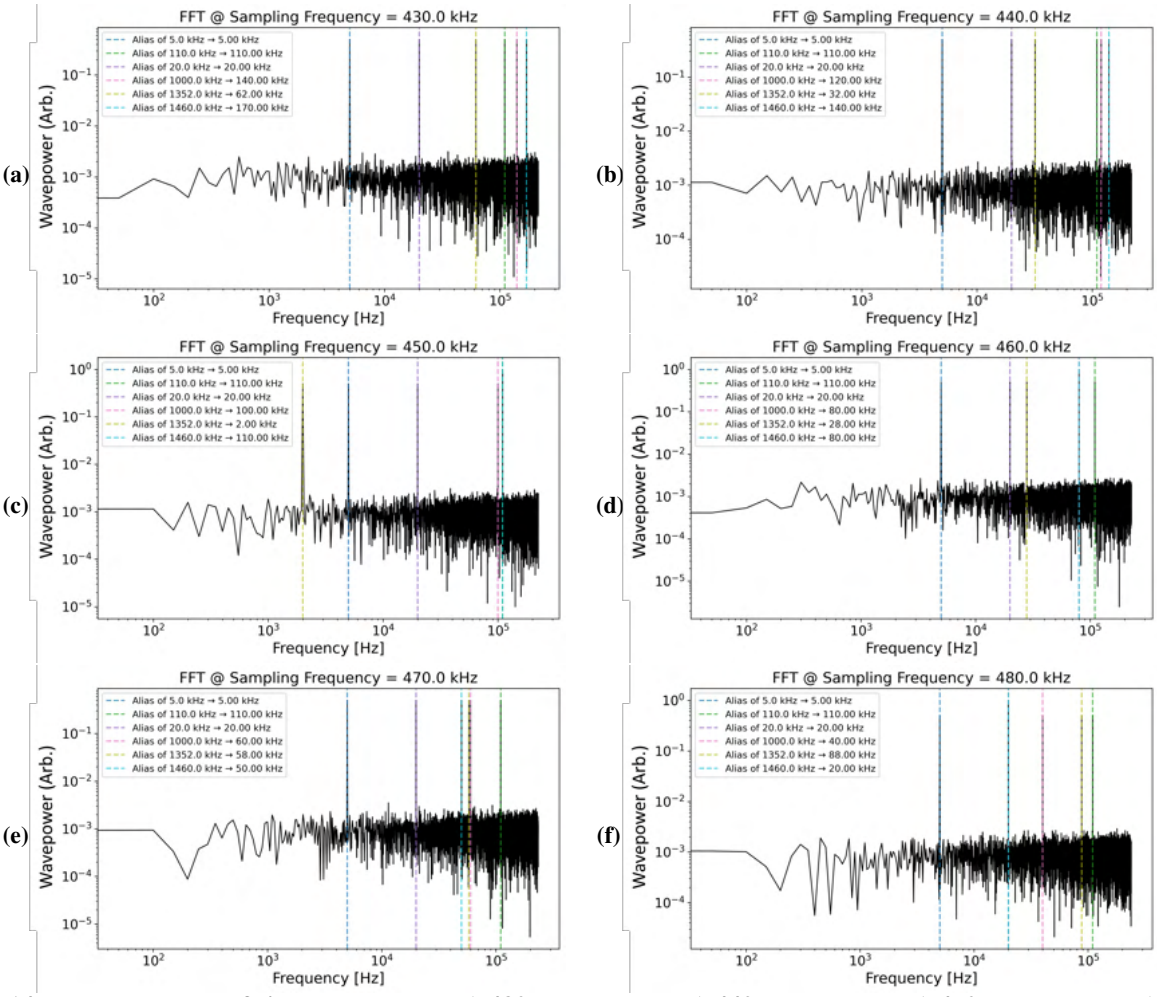

Fig. 14 Power spectra of simulated waves: a) 430 kHz dataset, b) 440 kHz dataset, c) 450 kHz dataset, d) 460 kHz dataset, e) 470 kHz dataset, f) 480 kHz dataset

Taking the Fourier transform of the simulated signals at each sampling frequency and computing the wave power yields the six power spectra shown in Fig. 14. We see in each power spectra that there are three frequency peaks that do not vary across the sampling frequencies - these are the non-aliased modes we simulated. The three aliased modes change in frequency depending on the sampling rate, as expected. Overlaying these spectra on top of one another yields the plot in Fig. 15. Comparing this power spectra overlay to the one shown in 3c, it become evident that while manual selection of which frequencies to input into the temporal anti-aliasing framework is trivial in the case of Fig. 3c where there is only one choice per sampling frequency, the manual selection approach becomes intractable when there are multiple aliased frequencies present. In this case, when only considering three choices of frequency peaks per sampling frequency dataset, there are a total of $3^6 = 729$ unique combination of frequency peaks (when picking one frequency peak per sampling frequency dataset) to check through manually.

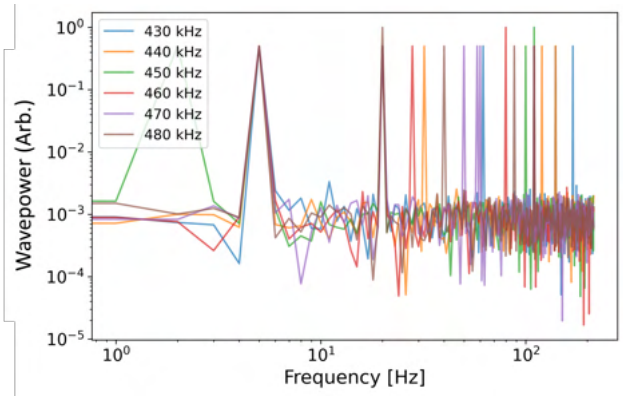

Fig. 15 Overlay of power spectra

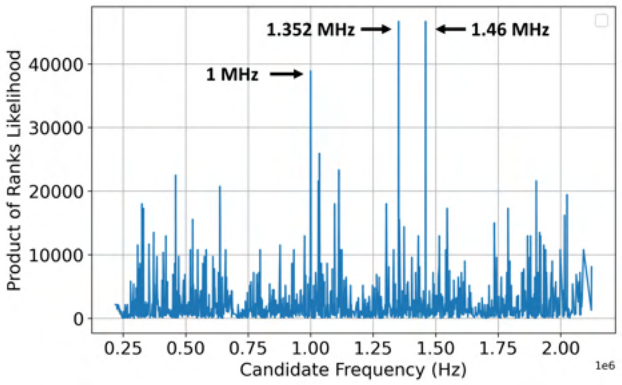

Fig. 16 Automatic temporal anti-aliasing likelihood

However, leveraging our automatic temporal anti-aliasing algorithm, we can quickly produce the likelihood plot shown in Fig. 16. Indeed, we see here that the algorithm has assigned the highest likelihood to the three aliased modes.

The disparity in likelihood between the three aliased modes can be attributed to a couple of frequency indices where more than one of the modes aliases to across the sampling frequency datasets. This can be seen most clearly in Fig. 15 near 100 kH, where the 450 kHz (green) and 480 kHz (maroon) datasets share a peak. Although this algorithm shows promise, more work will have to be done to improve the automatic temporal anti-aliasing algorithm to account for frequency aliasing that share a common folded frequency.

VI. Conclusion

In this work, we proposed and validated a temporal anti-aliasing framework for high-speed imaging (HSI) diagnostics that combines multiple datasets acquired at different sampling rates to infer modes propagating at frequencies beyond the Nyquist limit of high-speed cameras. Spectral analysis on five HSI datasets of the AEPS ETU-2 test article, taken at various framerates during operation at the 600 V, 12.5 kW condition in VF-5, yields several features associated with global and cathode modes, as well as sampling-frequency-dependent peaks, characteristic to temporally aliased frequencies. Next, applying the temporal anti-aliasing algorithm to these peaks suggests the presence of a 1.46 MHz global mode in the discharge. We compare this observed mode to other high-frequency modes reported in Hall thrusters and find that no 1.46 MHz narrow-band global mode has been reported in literature. Comparing this signal to the discharge current and voltage traces, there is a notable absence of a peak at 1.46 MHz. It is plausible that the signal could be attributed to experimental artifacts, and we discuss potential explanations to its detection in the context of confounding factors. We then make several recommendations on experimental design to differentiate real plasma effects from experimental artifacts. Finally, we proposed an improved version of the algorithm and presented promising preliminary results. Overall, this work demonstrates that temporal anti-aliasing can, in principle, extend the frequency bandwidth of HSI diagnostics beyond the Nyquist limit, enabling observation of high-frequency modes otherwise inaccessible to high-speed cameras.

Acknowledgments

This work was supported by a NASA Space Technology Graduate Research Opportunity (NSTGRO) Fellowship (80NSSC24K1331), the University of Michigan Rackham Graduate School Rackham Merit Fellowship (RMF), and the U.S. Department of Energy, Office of Science, Office of Fusion Energy Sciences, under the Early Career Research Program Award, DE-SC0022988.

Appendix

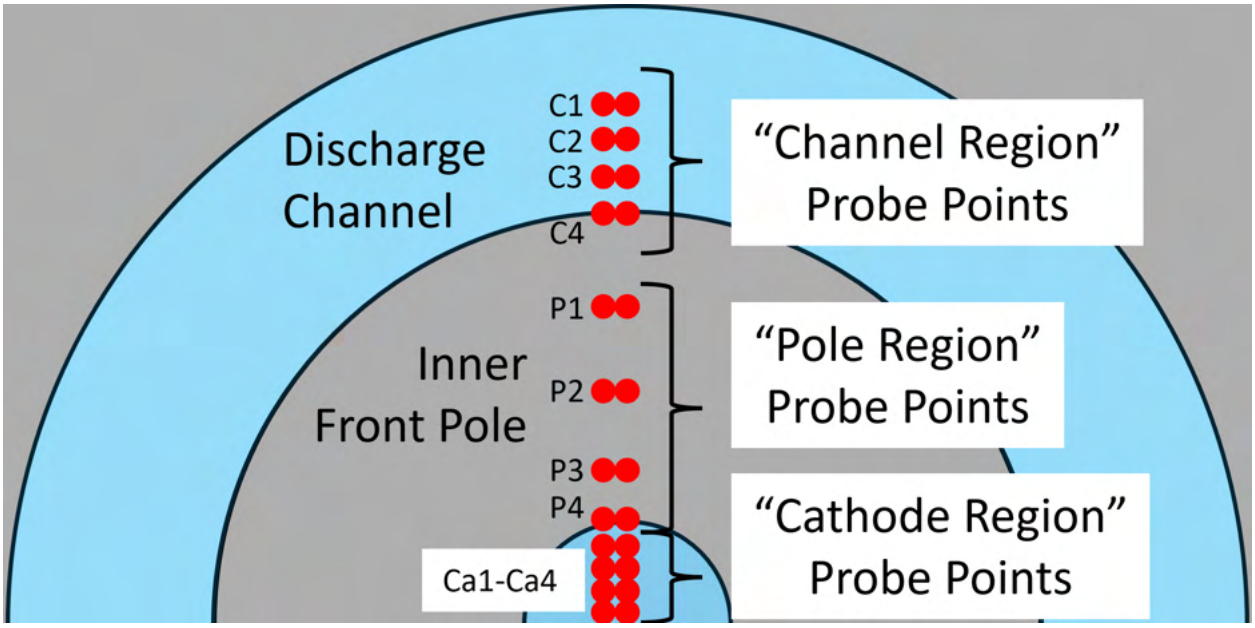

Fig. 17 Appendix Reference for All Radial Locations Probed on Imaging Domain

A. 480 kHz HSI dataset

1. 480 kHz dataset: channel region

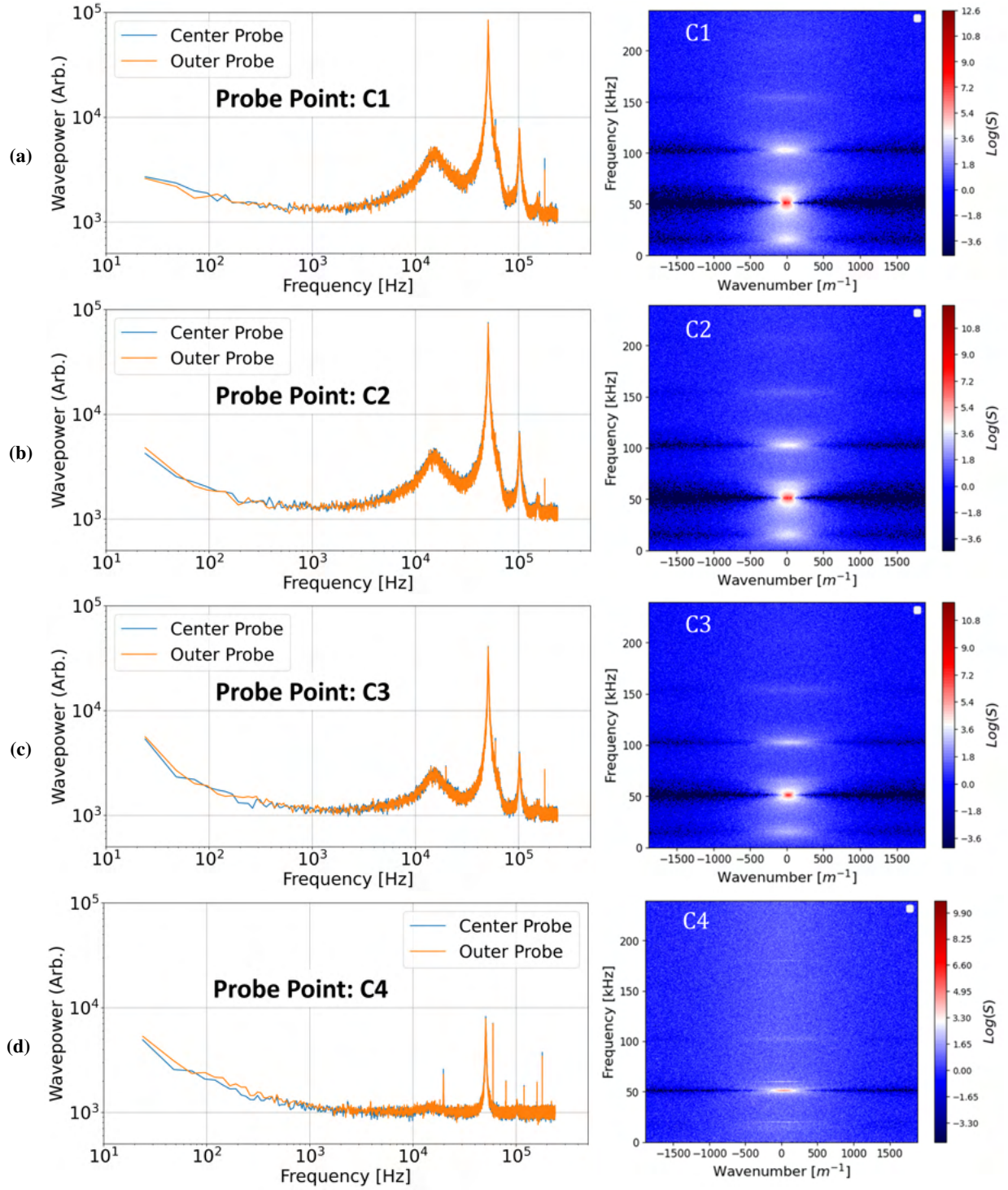

Fig. 18 480 kHz dataset channel region spatially-resolved power spectra and Beall plots: a) Point C1, b) Point C2, c) Point C3, d) Point C4

2. 480 kHz dataset: pole region

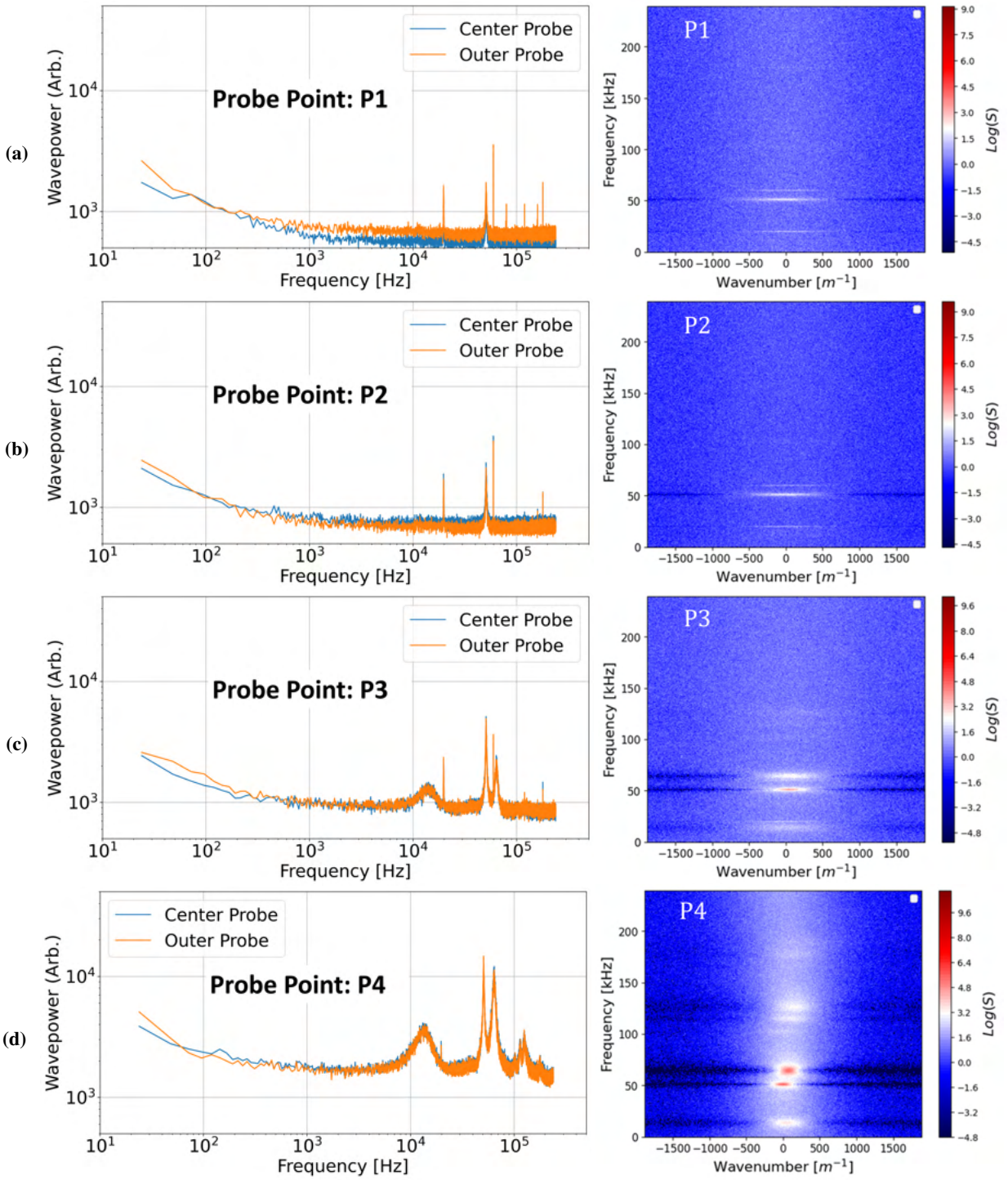

Fig. 19 480 kHz dataset pole region spatially-resolved power spectra and Beall plots: a) Point C1, b) Point C2, c) Point C3, d) Point C4

3. 480 kHz dataset: cathode region

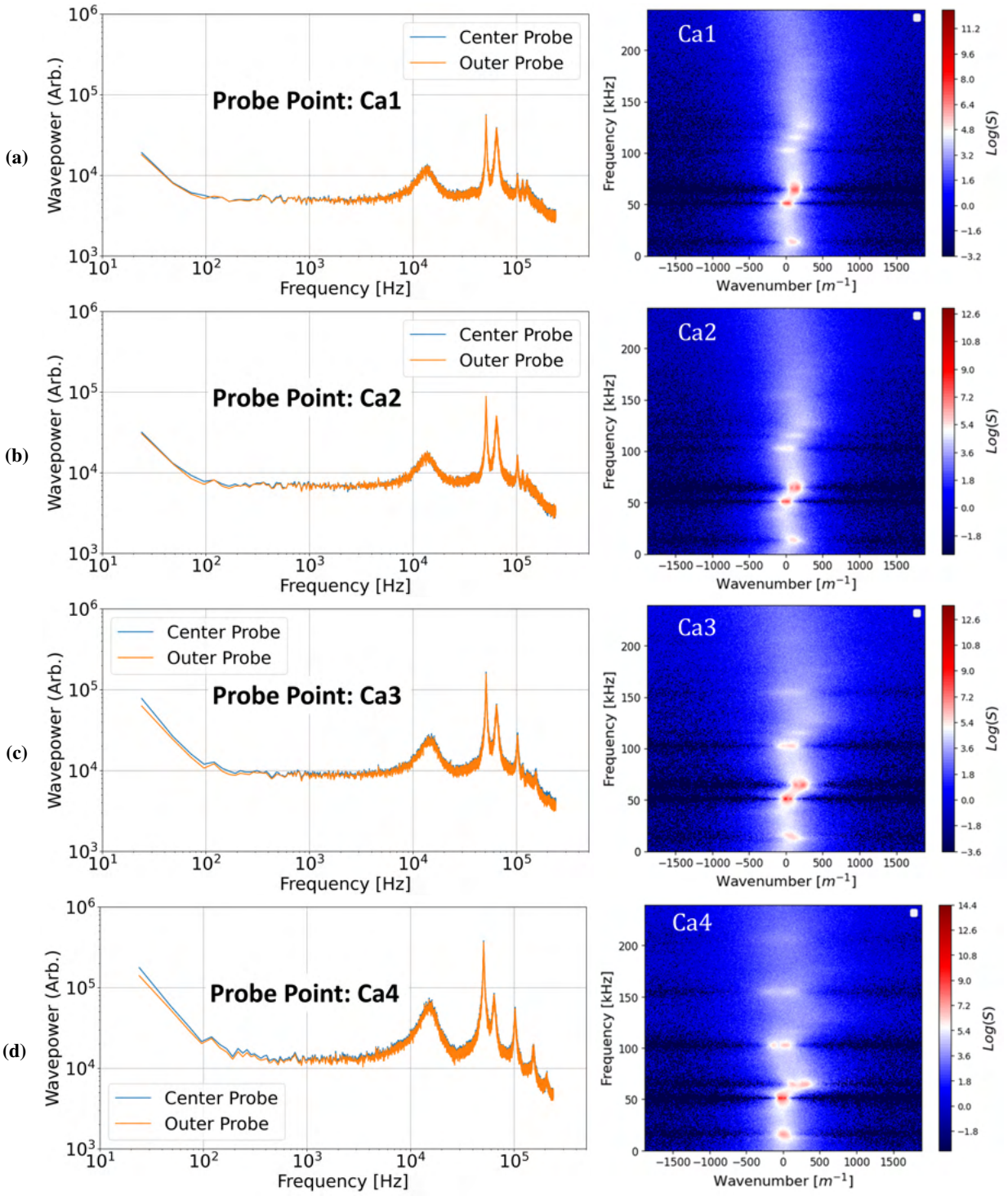

Fig. 20 480 kHz dataset cathode region spatially-resolved power spectra and Beall plots: a) Point C1, b) Point C2, c) Point C3, d) Point C4

SECTION

B. 450 kHz HSI dataset

1. 450 kHz dataset: channel region

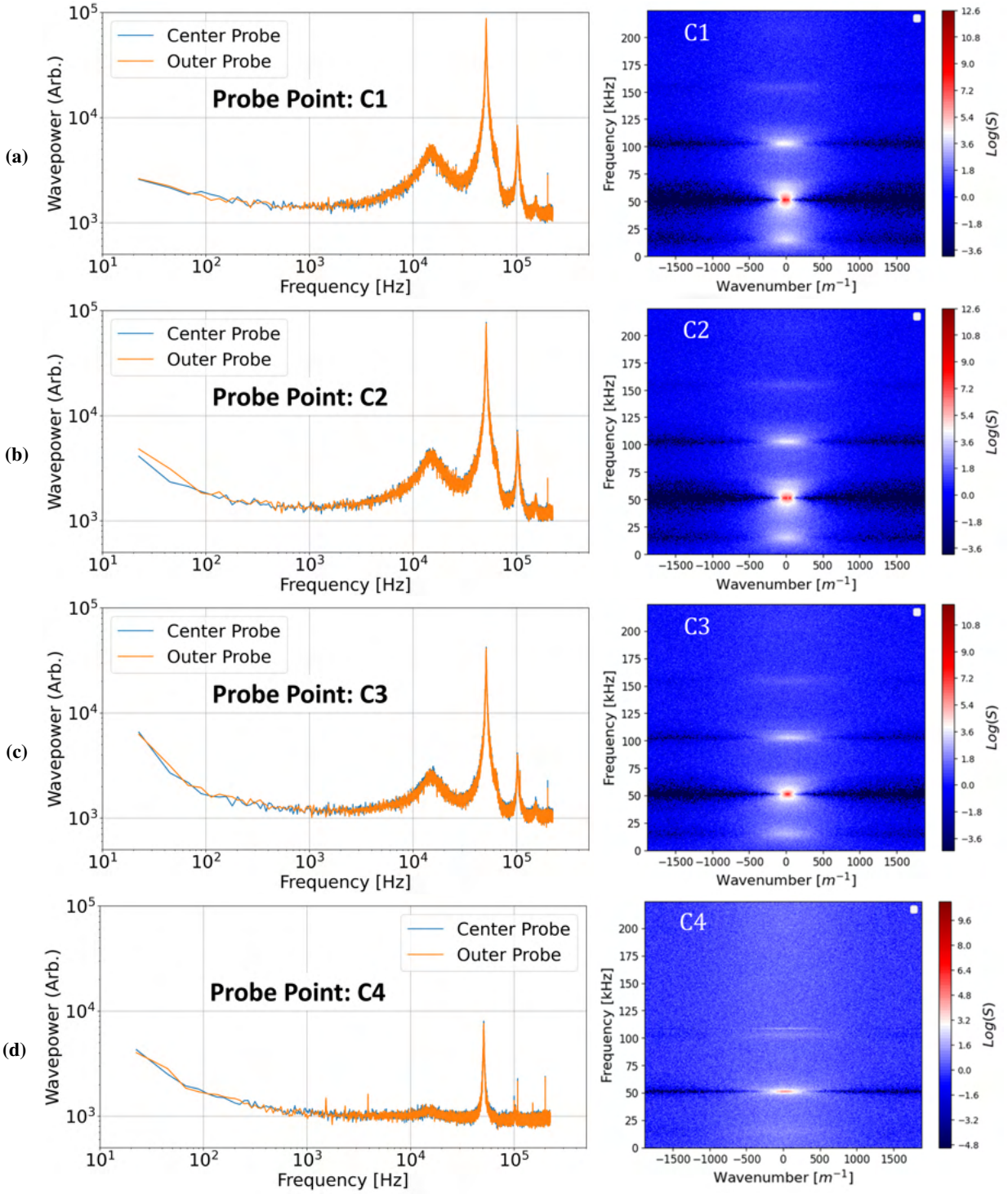

Fig. 21 450 kHz dataset channel region spatially-resolved power spectra and Beall plots: a) Point C1, b) Point C2, c) Point C3, d) Point C4

2. 450 kHz dataset: pole region

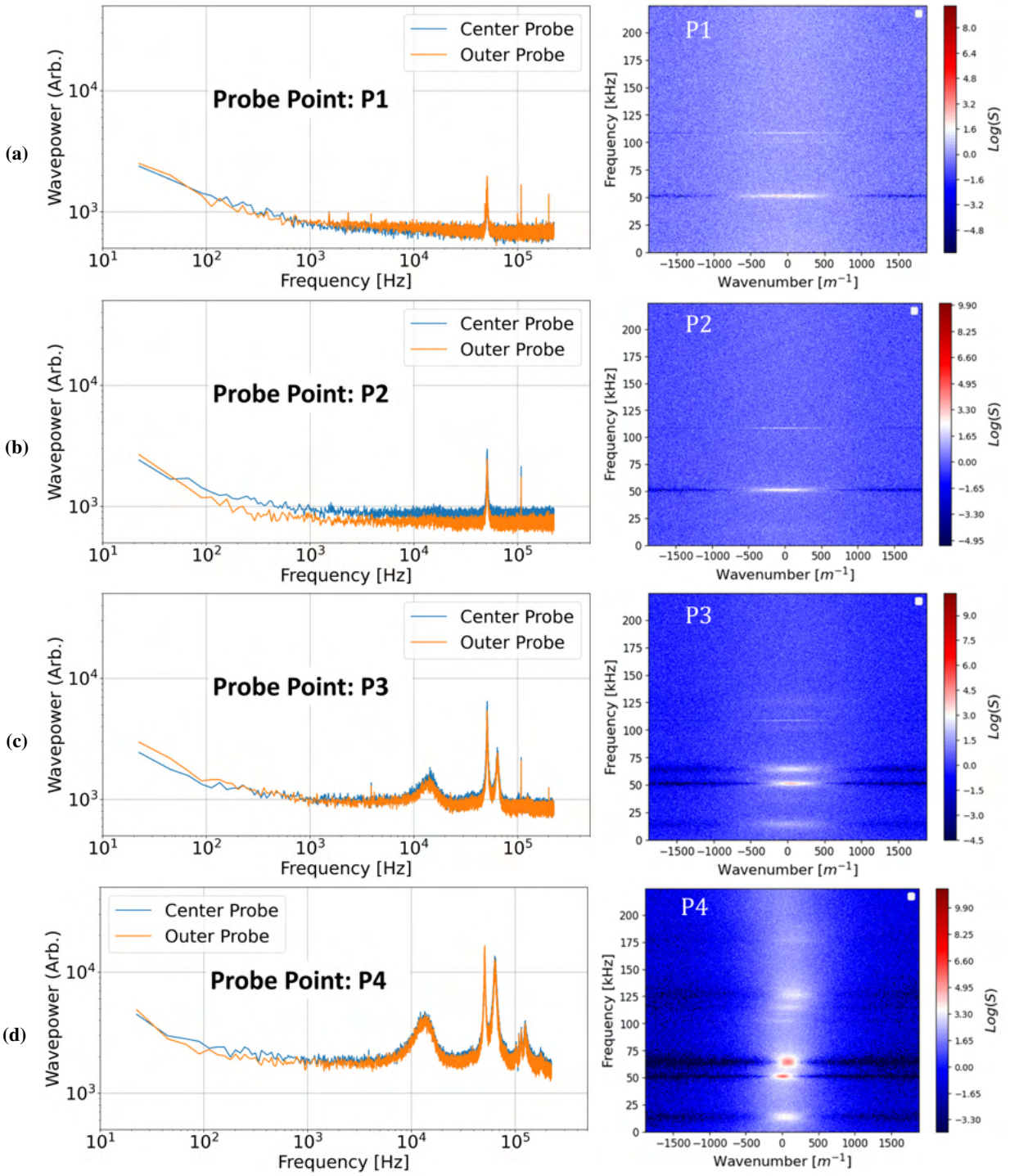

Fig. 22 450 kHz dataset pole region spatially-resolved power spectra and Beall plots: a) Point C1, b) Point C2, c) Point C3, d) Point C4

3. 450 kHz dataset: cathode region

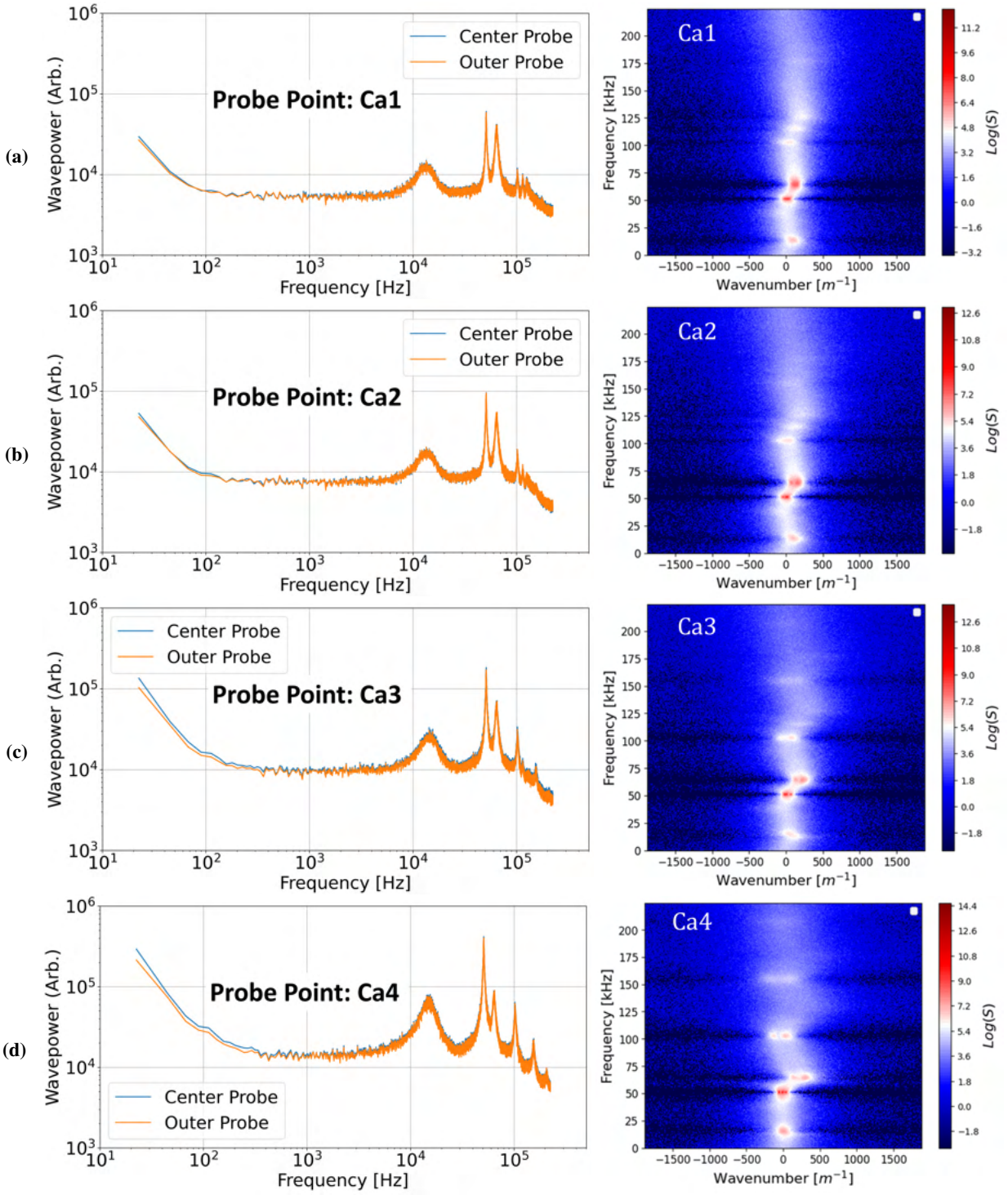

Fig. 23 450 kHz dataset cathode region spatially-resolved power spectra and Beall plots: a) Point C1, b) Point C2, c) Point C3, d) Point C4

SECTION

C. 400 kHz HSI dataset

1. 400 kHz dataset: channel region

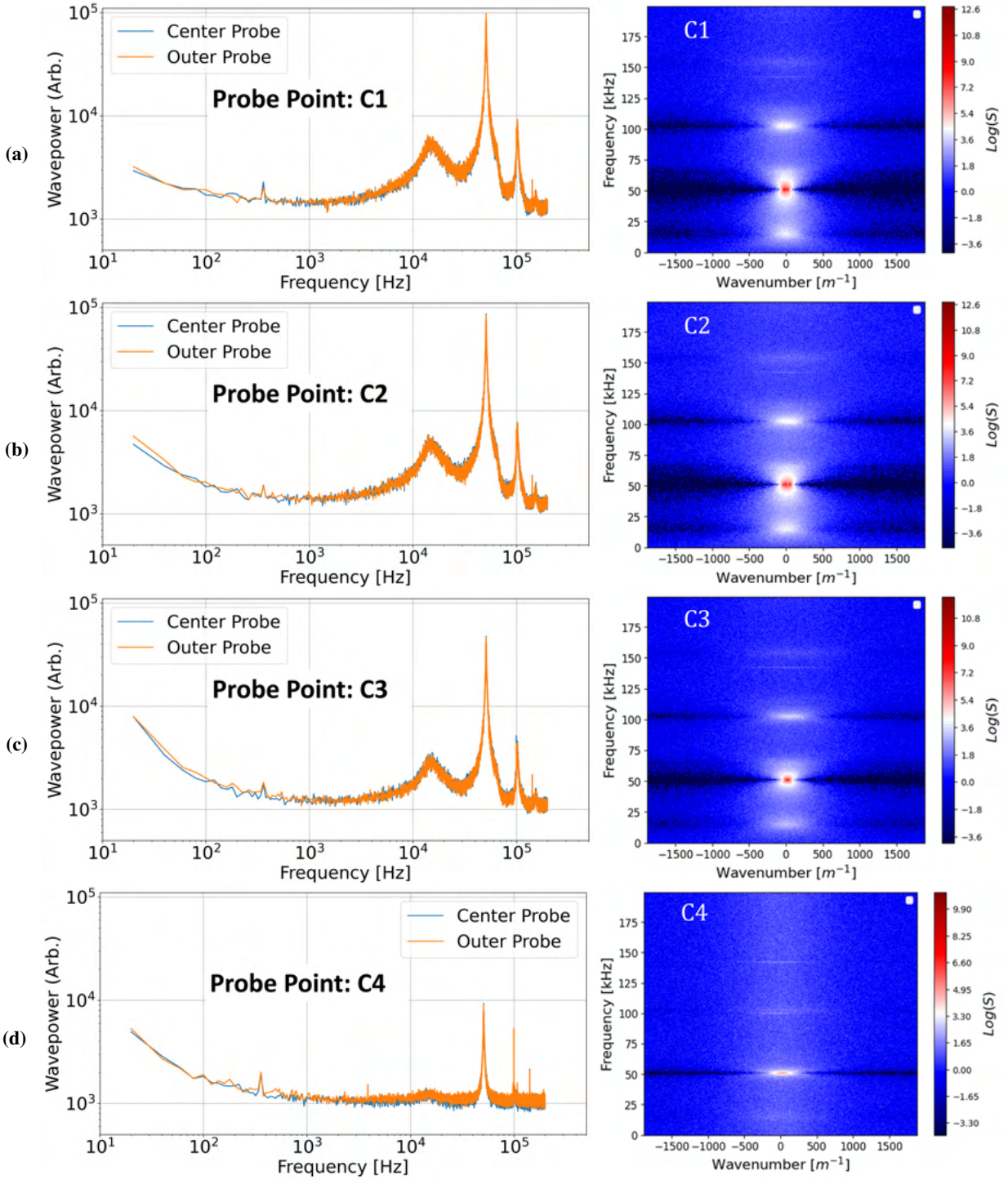

Fig. 24 400 kHz dataset channel region spatially-resolved power spectra and Beall plots: a) Point C1, b) Point C2, c) Point C3, d) Point C4

2. 400 kHz dataset: pole region

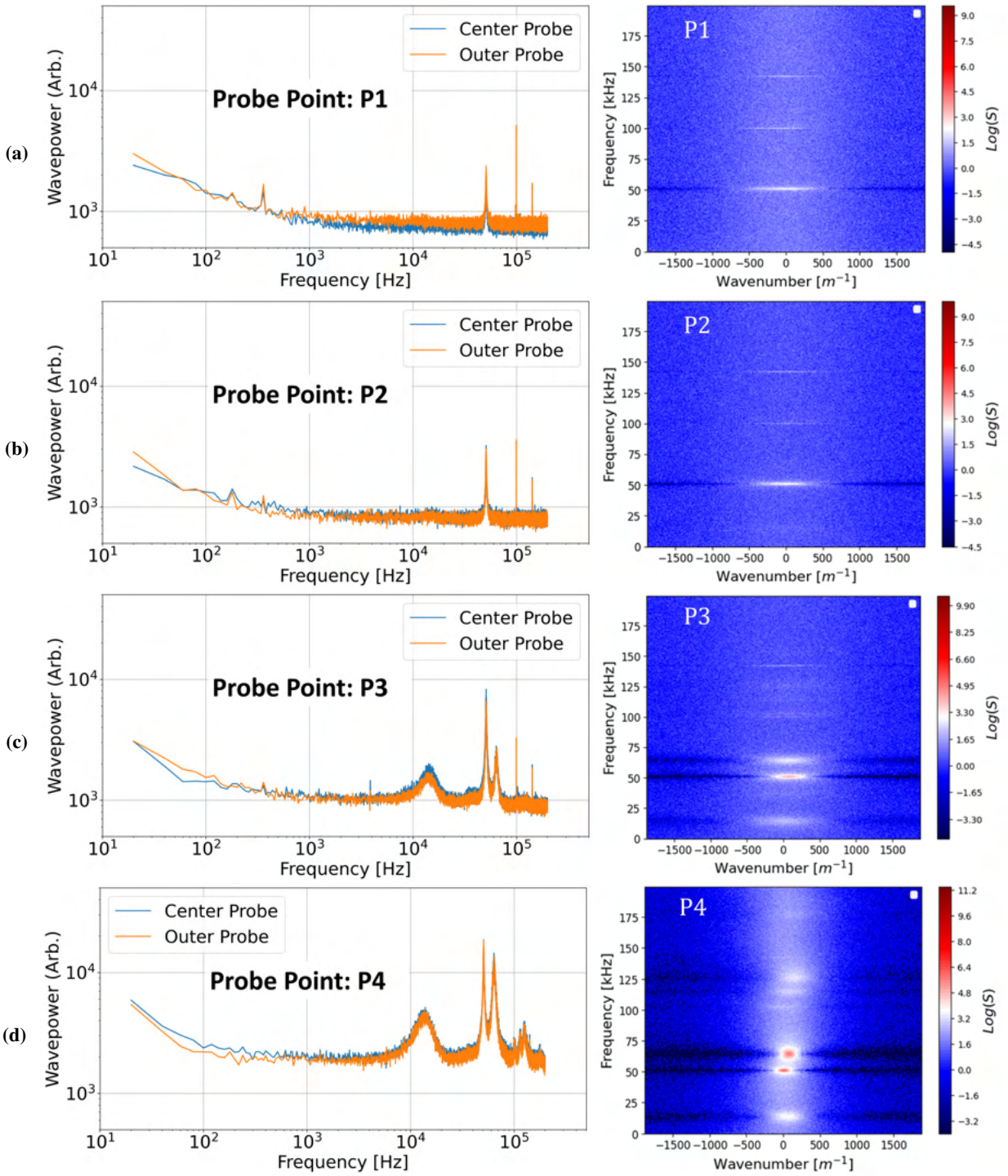

Fig. 25 400 kHz dataset pole region spatially-resolved power spectra and Beall plots: a) Point C1, b) Point C2, c) Point C3, d) Point C4

3. 400 kHz dataset: cathode region

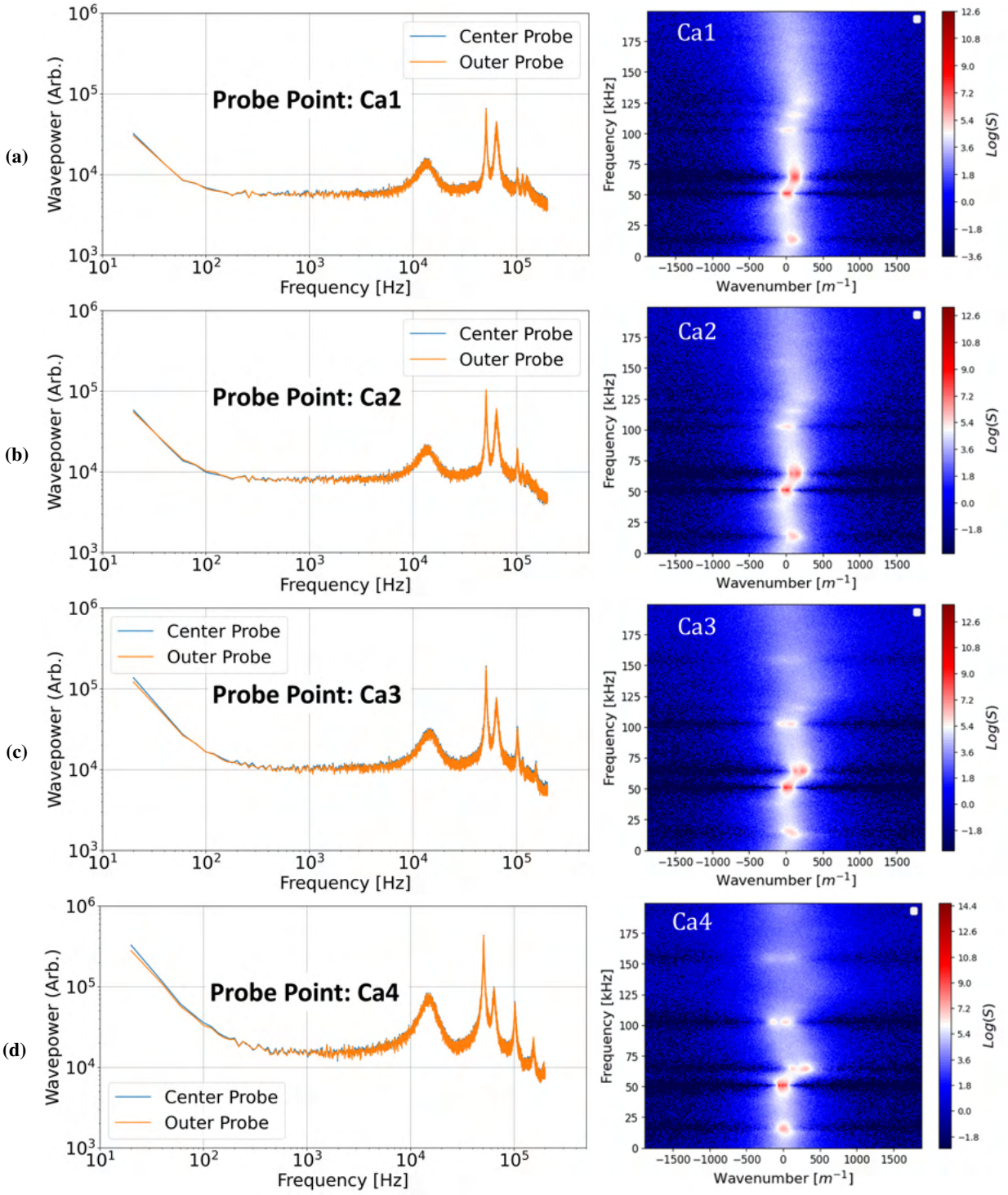

Fig. 26 400 kHz dataset cathode region spatially-resolved power spectra and Beall plots: a) Point C1, b) Point C2, c) Point C3, d) Point C4

SECTION

D. 360 kHz HSI dataset

1. 360 kHz dataset: channel region

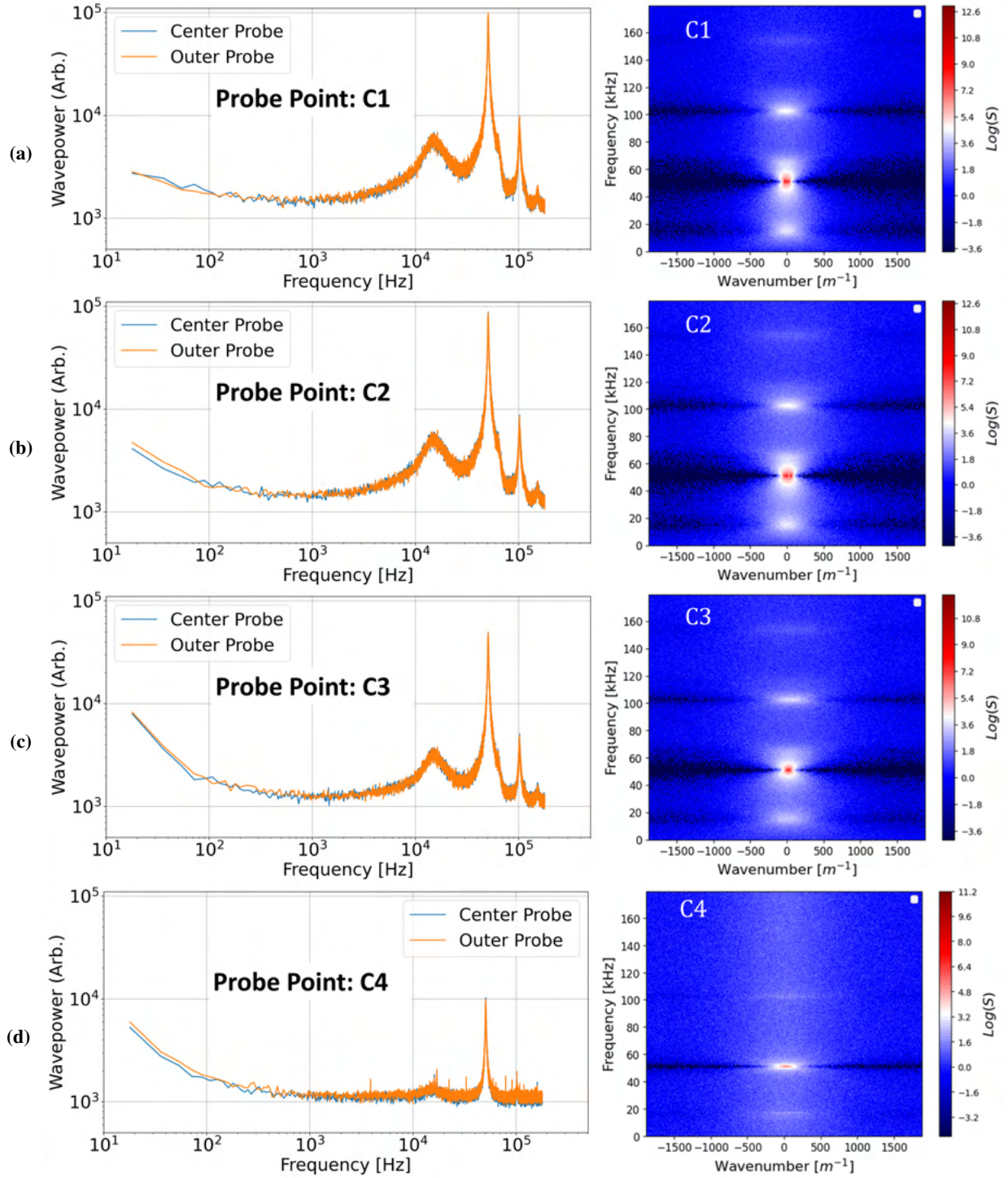

Fig. 27 360 kHz dataset channel region spatially-resolved power spectra and Beall plots: a) Point C1, b) Point C2, c) Point C3, d) Point C4

2. 360 kHz dataset: pole region

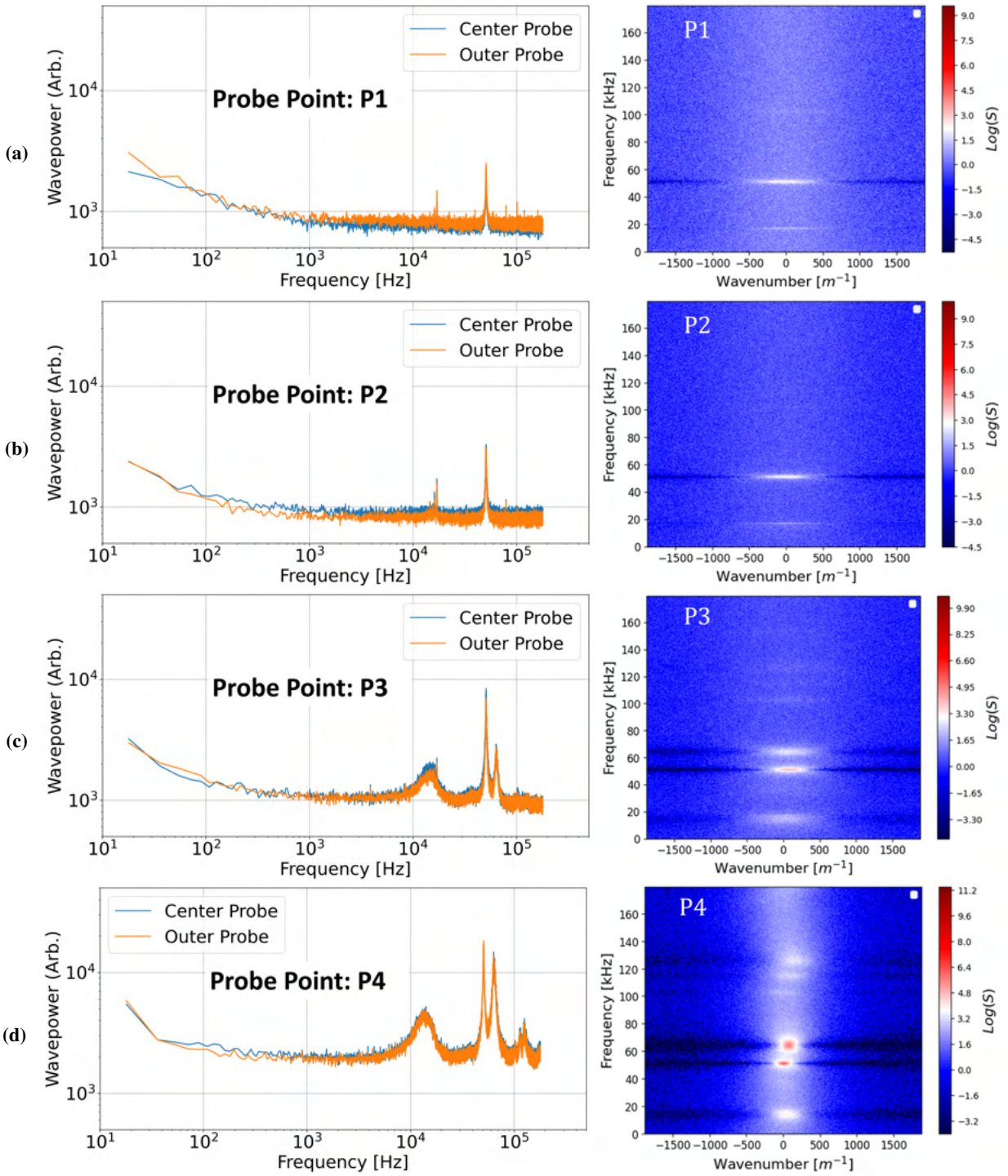

Fig. 28 360 kHz dataset pole region spatially-resolved power spectra and Beall plots: a) Point C1, b) Point C2, c) Point C3, d) Point C4

3. 360 kHz dataset: cathode region

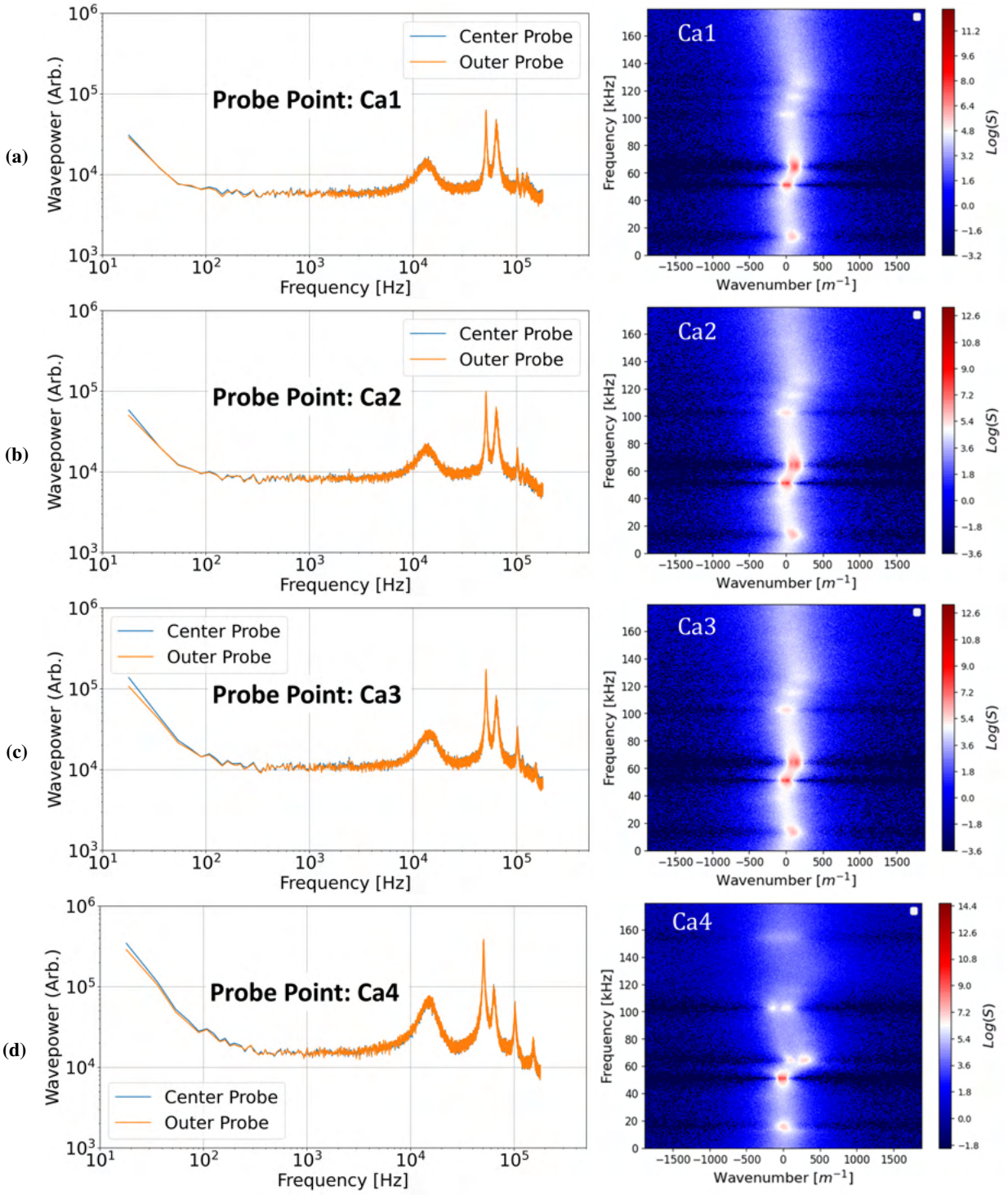

Fig. 29 360 kHz dataset cathode region spatially-resolved power spectra and Beall plots: a) Point C1, b) Point C2, c) Point C3, d) Point C4

SECTION

E. 350 kHz HSI dataset

1. 350 kHz dataset: channel region

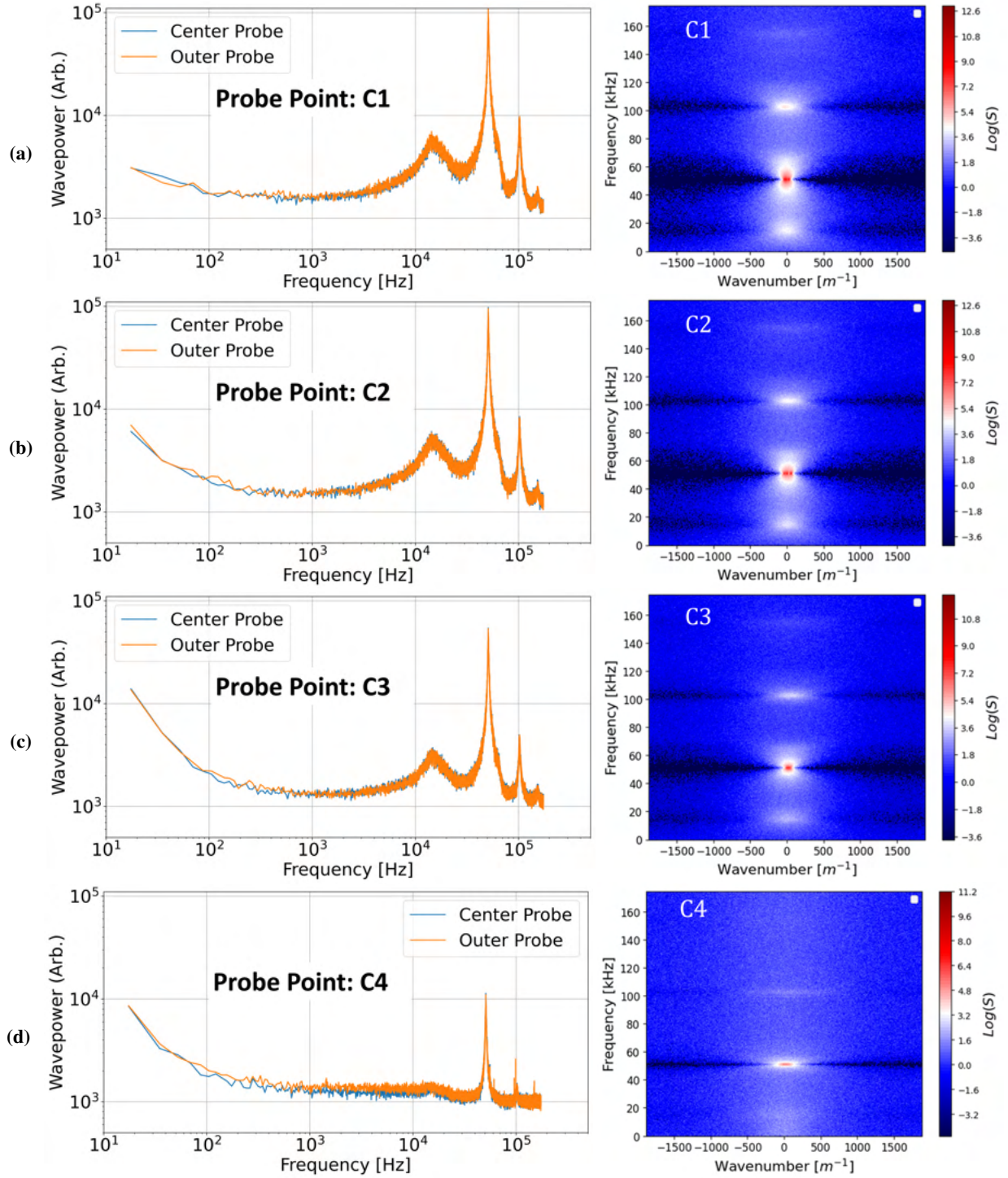

Fig. 30 350 kHz dataset channel region spatially-resolved power spectra and Beall plots: a) Point C1, b) Point C2, c) Point C3, d) Point C4

2. 350 kHz dataset: pole region

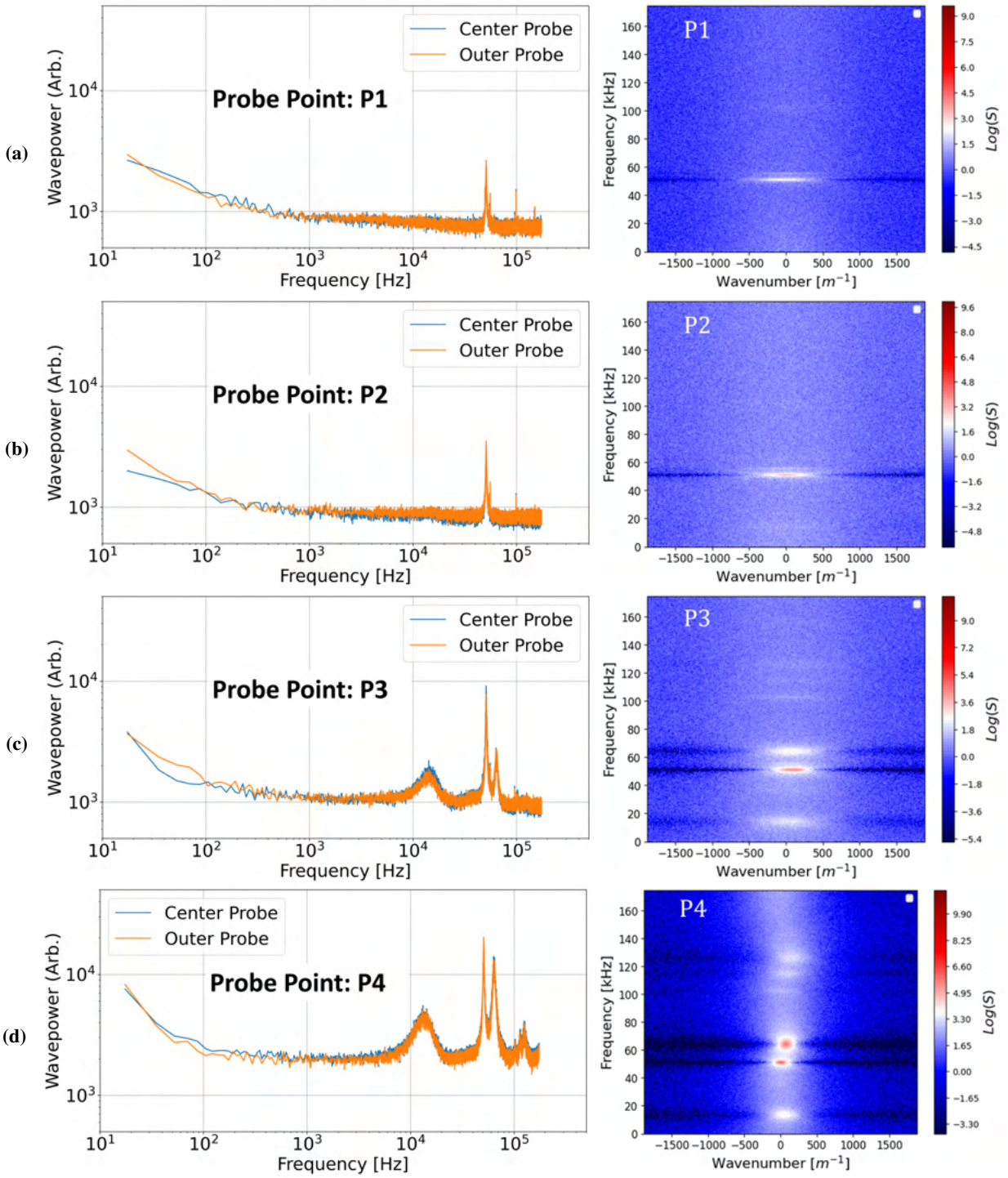

Fig. 31 350 kHz dataset pole region spatially-resolved power spectra and Beall plots: a) Point C1, b) Point C2, c) Point C3, d) Point C4

3. 350 kHz dataset: cathode region

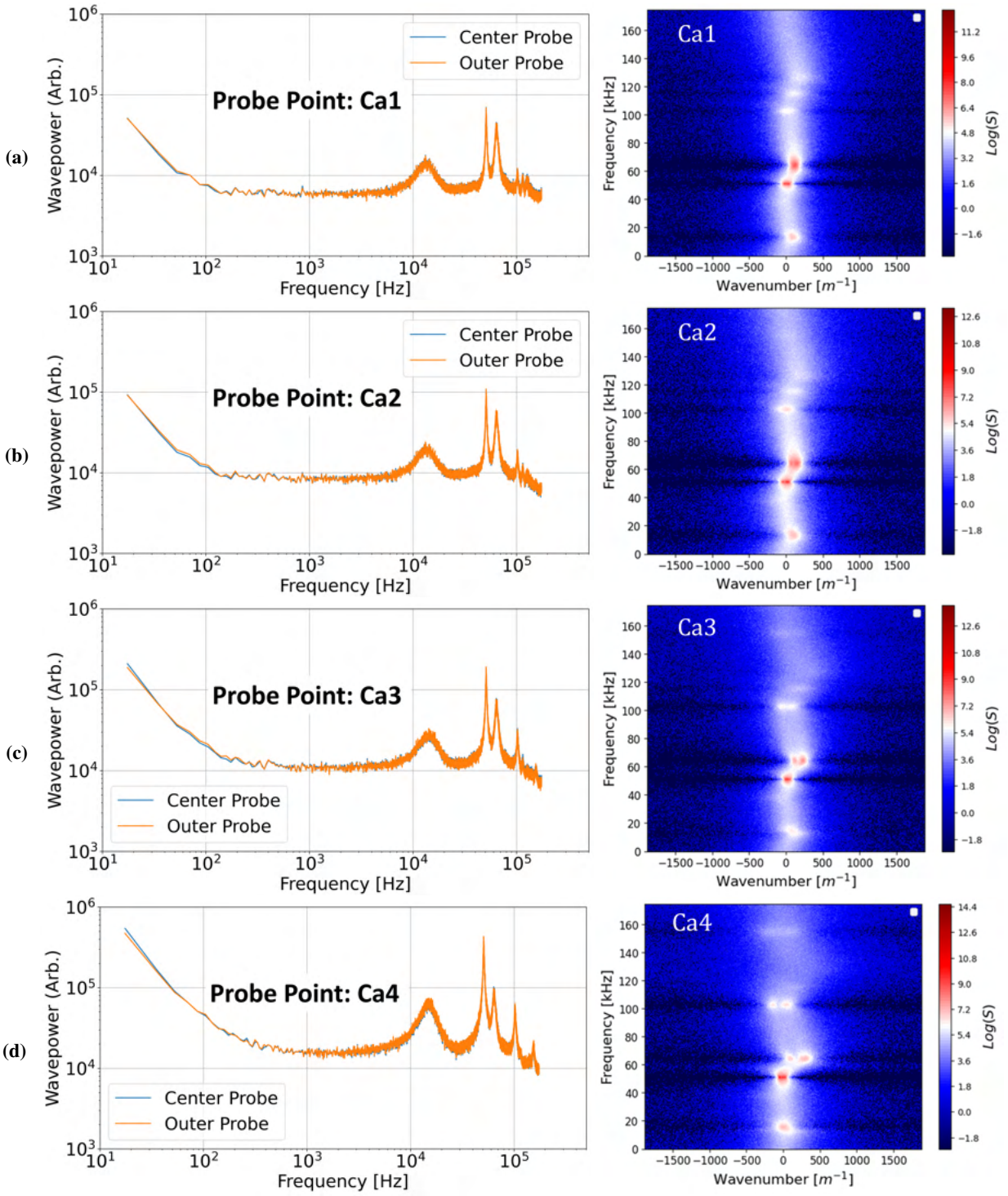

Fig. 32 350 kHz dataset cathode region spatially-resolved power spectra and Beall plots: a) Point C1, b) Point C2, c) Point C3, d) Point C4

References

[1] McDonald, M. S., "Electron Transport in Hall Thrusters," Dissertation, 2012. https://doi.org/null.

[2] Huang, W., Kamhawi, H., and Haag, T. W., "Plasma Oscillation Characterization of NASA's HERMeS Hall Thruster via High Speed Imaging," 52nd AIAA/SAE/ASEE Joint Propulsion Conference, 2016. https://doi.org/10.2514/6.2016-4829.

[3] Georgin, M. P., Byrne, M., Jorns, B. A., and Gallimore, A. D., "Passive High-speed Imaging of Ion Acoustic Turbulence in a Hollow Cathode," 53rd AIAA/SAE/ASEE Joint Propulsion Conference, 2017. https://doi.org/10.2514/6.2017-4973.

[4] Baird, M. J., "Investigating Newly Discovered Oscillation Modes in Magnetically Shielded Hall Effect Thrusters Utilizing High Speed Diagnostics," Dissertation, 2020. https://doi.org/null.

[5] Brooks, J. W., Kaptanoglu, A. A., and McDonald, M., "A comparison of Fourier and POD mode decomposition methods for high-speed Hall thruster video," Frontiers in Space Technologies, 2023. https://doi.org/10.3389/frspt.2023.1220011.

[6] Choueiri, E. Y., and Choueiri, E. Y., "Plasma oscillations in Hall thrusters," Physics of Plasmas, 2001. https://doi.org/10.1063/1.1354644.

[7] Brown, Z. A., and Jorns, B. A., "Growth and Saturation of the Electron Drift Instability in a Crossed Field Plasma," Phys. Rev. Lett., Vol. 130, 2023, p. 115101. https://doi.org/10.1103/PhysRevLett.130.115101.

[8] Mikellides, I. G., Lopez Ortega, A., and Chaplin, V. H., "Theory of the anomalous momentum exchange from wave–particle interactions in Hall-effect ion accelerators and comparisons with measurements," Physics of Fluids, Vol. 36, No. 7, 2024, p. 074121. https://doi.org/10.1063/5.0213605.

[9] Jorns, B. A., Mikellides, I. G., and Goebel, D. M., "Ion acoustic turbulence in a 100-A LaB_6 hollow cathode," Phys. Rev. E, Vol. 90, 2014, p. 063106. https://doi.org/10.1103/PhysRevE.90.063106.

[10] Mooney, M. M., and Lemmer, K. M., "The effect of probe separation distance on the analysis of plasma waves in a cathode plasma," AIAA SCITECH 2024 Forum, 2024. https://doi.org/10.2514/6.2024-0923.

[11] Liu, M. F., and Jorns, B. A., "Experimental Measurements of the Dispersion and Growth Rate of Ion Acoustic Waves in the Plume of a Hollow Cathode," 38th International Electric Propulsion Conference, 2024.

[12] Brown, Z., Brown, Z., Jorns, B., and Jorns, B., "Experimental measurements of the contribution of plasma turbulence to anomalous collision frequency in a Hall thruster," AIAA Propulsion and Energy 2021 Forum, 2021. https://doi.org/10.2514/6.2021-3415.

[13] Liu, M. F., and Jorns, B. A., "Anti-aliasing Technique for Inferring Dispersion of Short-wavelength Instabilities in Electric Propulsion Devices," AIAA SCITECH 2025 Forum, 2025. https://doi.org/10.2514/6.2025-1293.

[14] Whittaker, E. T., "XVIII.—On the Functions which are represented by the Expansions of the Interpolation-Theory," Proceedings of the Royal Society of Edinburgh, Vol. 35, 1915, p. 181–194. https://doi.org/10.1017/S0370164600017806.

[15] Nyquist, H., "Certain topics in telegraph transmission theory," Proceedings of the IEEE, Vol. 90, No. 2, 2002, pp. 280–305. https://doi.org/10.1109/5.989875.

[16] Shannon, C., "Communication In The Presence Of Noise," Proceedings of the IEEE, Vol. 86, No. 2, 1998, pp. 447–457. https://doi.org/10.1109/JPROC.1998.659497.

[17] Oppenheim, A., and Schafer, R., Discrete-Time Signal Processing, Pearson Deutschland, 2013. URL https://elibrary.pearson.de/book/99.150005/9781292038155.

[18] Shastry, R., Kamhawi, H., Frieman, J. D., Soulas, G. C., Gray, T., Verhey, T. R., Kachele, C. D., Williams, G., Simmons, N. C., Lobbia, R. B., Arestie, S., Chaplin, V. H., Fisher, J., Blackner, G., Forbes, E., Hondagneu, J., Branch, N., Zubair, J., and Watts, H., "12-kW advanced electric propulsion system hall current thruster qualification and production status," Journal of Electric Propulsion, 2025.

[19] J. D. Frieman, e. a., "Performance of the 12.5-kW Advanced Electric Propulsion System Engineering Test Unit Hall Thruster," 68th Joint Army-Navy-NASA-Air Form (JANNAF) Propulsion Meeting, 2021. URL https://ntrs.nasa.gov/citations/20210015721.

[20] Liu, M. F., and Jorns, B. A., "Experimental Validation of a Spatial Anti-aliasing Plasma Wave Analaysis Technique on Ion Acoustic Turbulence in a Hollow Cathode Plume," 39th International Electric Propulsion Conference, 2025.

[21] Beall, J. M., Kim, Y. C., and Powers, E. J., "Estimation of wavenumber and frequency spectra using fixed probe pairs," Journal of Applied Physics, 1982. https://doi.org/10.1063/1.331279.

[22] Jorns, B. A., and Hofer, R. R., "Plasma oscillations in a 6-kW magnetically shielded Hall thruster," Physics of Plasmas, Vol. 21, No. 5, 2014, p. 053512. https://doi.org/10.1063/1.4879819, URL https://doi.org/10.1063/1.4879819.

[23] Tsikata, S., Lemoine, N., Pisarev, V., and Grésillon, D. M., "Dispersion relations of electron density fluctuations in a Hall thruster plasma, observed by collective light scattering," Physics of Plasmas, Vol. 16, No. 3, 2009, p. 033506. https://doi.org/10.1063/1.3093261, URL https://doi.org/10.1063/1.3093261.

[24] Barral, S., Makowski, K., Peradzyński, Z., and Dudeck, M., "Transit-time instability in Hall thrusters," Physics of Plasmas, Vol. 12, No. 7, 2005, p. 073504. https://doi.org/10.1063/1.1947796, URL https://doi.org/10.1063/1.1947796.

[25] Charoy, T., Lafleur, T., Laguna, A. A., Bourdon, A., and Chabert, P., "The interaction between ion transit-time and electron drift instabilities and their effect on anomalous electron transport in Hall thrusters," Plasma Sources Science and Technology, Vol. 30, No. 6, 2021, p. 065017. https://doi.org/10.1088/1361-6595/ac02b3, URL https://doi.org/10.1088/1361-6595/ac02b3.

[26] Delavière—Delion, Q., Gaboriau, F., Fubiani, G., and Garrigues, L., "Experimental observation of low-frequency interactions at different scales and evidence of transit time oscillations in a Hall thruster: Spectral analysis," Physics of Plasmas, Vol. 31, No. 7, 2024, p. 072110. https://doi.org/10.1063/5.0206369, URL https://doi.org/10.1063/5.0206369.